

Astrophysical Neutrino Event Rates and Sensitivity for Neutrino Telescopes

Ivone F. M. Albuquerque

Department of Astronomy and Space Sciences Laboratory, University of California, Berkeley, CA 94720.

IFAlbuquerque@lbl.gov

Jodi Lamoureux

National Energy Research Scientific Computing Center, Lawrence Berkeley National Laboratory, Berkeley, CA 94720.

JILamoureux@lbl.gov

and

George F. Smoot

Lawrence Berkeley National Laboratory, Space Sciences Laboratory and Department of Physics, University of California, Berkeley, CA 94720.

GFSmoot@lbl.gov

ABSTRACT

Spectacular processes in astrophysical sites produce high-energy cosmic rays which are further accelerated by Fermi-shocks into a power-law spectrum. These, in passing through radiation fields and matter, produce neutrinos. Neutrino telescopes are designed with large detection volumes to observe such astrophysical sources. A large volume is necessary because the fluxes and cross-sections are small. We estimate various telescopes' sensitivity and expected event rates from astrophysical sources of high-energy neutrinos. We find that an ideal detector of km^2 incident area can be sensitive to a flux of neutrinos integrated over energy from 10^5 and 10^7 GeV as low as $1.3 \times 10^{-8} \text{E}^{-2} (\text{GeV}/\text{cm}^2 \text{ s sr})$ which is three times smaller than the Waxman-Bachall conservative upper limit on potential neutrino flux. Detection from point sources is possible from known bursts and unlikely if there is no prior knowledge of the location and time of the burst. A real detector will have degraded performance.

Subject headings: Neutrino flux. Neutrino detection. Neutrino detection rates.

1. Introduction

Galactic and extra-galactic high-energy cosmic rays are observed at the Earth and in space through indicators such as synchrotron emission and gamma-radiation. Some of the most spectacular sites for their origin are the double-lobed radio sources associated with Active Galactic Nuclei. Figure 1 shows a compilation (Gaisser 2000) of the observed cosmic ray spectrum observed at the Earth.

These high-energy cosmic rays interact with radiation or matter at the acceleration sites, in transit through intergalactic and interstellar space, and in the Earth’s atmosphere. Often the result of this interaction is the production of pions, kaons, and other particles that decay into muons and an associated muon neutrino. The muon will usually decay into an electron, an electron neutrino and a muon neutrino. Each primary cosmic ray interaction typically would produce at least three neutrinos and could produce substantially more.

One can estimate the flux of such neutrinos by models and from observations of the cosmic ray fluxes. One has to take into account the cosmic ray interactions which at high energies and from distant sources are primarily with photons. These estimates and fluxes must satisfy the limits set by the observations of cosmic rays. In this paper we estimate the muon neutrino and secondary muon flux from diffuse and point sources. Here we do not account for the flux due to exotic and beyond standard model possibilities but leave those topics for a later paper. A review of neutrino physics within and beyond the standard model can be found in (Learned and Mannheim 2000).

In Part II we review and examine estimates of high energy neutrino fluxes and upper limits from diffuse and point sources. This reviews the work of Waxman and Bahcall (Waxman 1995; Waxman and Bahcall 1999; Bahcall and Waxman 1999), of Mannheim, Protheroe and Rachen (Mannheim Protheroe and Rachen 2001) and the recent estimates by Gaisser (Gaisser 2000). In Part III we compile and compute the interaction rates, that is, the neutrino interactions per unit volume per unit time and the number of muons entering or appearing in a generic detector. This work is directly compared to estimates by Gaisser (Gaisser 2000). We include the fundamental physics aspects of instrument performance to determine the experimental sensitivity of an ideal detector of km^2 incident area to astrophysical sources. This is done in a generic form such that in Part IV it can be translated to different detector geometries. A realistic event rate is then determined for different proposed detectors such as IceCube, AMANDA, ANTARES and NESTOR.

2. Neutrino Fluxes

2.1. Diffuse Flux

2.1.1. *Waxman and Bahcall Limit*

Waxman and Bahcall (WB) (Waxman and Bahcall 1999; Bahcall and Waxman 1999) pointed out that the observed cosmic ray flux at high energies implies an upper bound on the high-energy astrophysical neutrino flux. The latter is produced by the parent cosmic ray particles through pion production.

This argument holds for sources that are “optically thin” to the primary cosmic rays. “Optically thin” sources are those for which the majority of the protons escape and only a fraction interact inside the source. Observations of primary cosmic ray flux then set a limit on the cosmic production rate of high-energy protons and in turn on the production rate of neutrinos.

Waxman and Bahcall also account for the cosmological evolution of cosmic ray fluxes. If the cosmic ray acceleration sites were much more active in the past (billions of years) than in the present (last 100 million years), then the flux of “cosmological” high-energy neutrinos could be enhanced.

In determining a limit for the diffuse neutrino flux, WB assume that all the proton energy is transferred to the pion when actually this energy transfer is typically about 20%. Due to this factor, they point out that their upper bound exceeds what can be observed by at least a factor of five.

One can conclude that if the WB limit holds, the neutrino flux upper bound can guide neutrino telescope designs. Neutrino telescopes should be designed to detect realistic fluxes which would be at a level well below the WB limit.

The key parameter in setting an upper limit for the neutrino flux from the collection of “optically thin” sources, is the primary cosmic ray spectral index (which is the power in the power law energy distribution). For the relativistic shocks needed to produce the very highest energy cosmic rays the spectral index is in the range 2 to 2.5 with a theoretical preference for 2 to 2.25 (Bell 1978; Blanford and Ostriker 1978). Either will adequately explain what appears to be the extra-galactic component of the cosmic rays as shown in Figure 1.

Waxman (Waxman 1995) has shown that the cosmic ray energy spectrum for energies between 10^{19} and 10^{20} eV is consistent with what is expected from a homogeneous cosmological distribution of cosmic ray sources and constrain the spectral index to be in the 1.8 –

2.8 range.

Fixing the spectral index to 2, WB (Waxman and Bahcall 1999) determine the limit on muon neutrino plus muon anti-neutrino flux to be

$$\left(\frac{d\phi_\nu}{dE}\right)_{\text{limit}} = \frac{1 \text{ to } 4 \times 10^{-8}}{E^2} \text{ GeV cm}^{-2}\text{s}^{-1}\text{sr}^{-1} \quad (1)$$

where ϕ_ν is the neutrino flux. The range in the coefficient depends upon what evolution is assumed. For this discussion we use the highest value and obtain an upper limit on the muon neutrino flux of

$$\left(\frac{d\phi}{d\ln E}\right)_{\text{limit}} = \frac{4 \times 10^{-8}}{E} \text{ cm}^{-2}\text{s}^{-1}\text{sr}^{-1} \quad (2)$$

The WB limit is shown in Figure 2.

2.1.2. Mannheim, Protheroe and Rachen limit

Mannheim, Protheroe and Rachen (MPR) (Mannheim Protheroe and Rachen 2001) determine an upper limit for diffuse neutrino sources in almost the same way as WB but with one important difference: they do not assume a specific cosmic ray spectrum but use the experimental upper limit on the extra-galactic proton contribution. While WB base their calculation on a cosmic ray flux with a single spectral index equal to 2, MPR define their spectrum based on current data at each energy.

MPR also extend their calculation for sources that are opaque (“optically thick”) to nucleons. For these sources they set an upper limit using the observed diffuse extra-galactic gamma-ray background assuming that the dominant part of the emitted gamma-radiation is in the Energetic Gamma Ray Experiment Telescope (EGRET) range.

Their results are also shown in Figure 2. Their limit for transparent (“thin”) sources is approximately the same as the WB limit for energies between 10^7 and 10^9 GeV and higher otherwise. Their limit allows the rates to be within the area defined by opaque and transparent sources. However, one should bear in mind that fluxes from opaque sources are difficult to produce. The interaction target in these sources must be optimized to allow interactions with most of the nucleons and at the same time allow pions and muons to decay. They also require an extraordinary larger energy budget than optically thin sources since a higher flux requires more energy. Also the opacity cuts down the flux of protons before

they reach useful high energies implying a much larger initial flux and energy budget than the simple order of magnitude more flux would imply. As MPR state in their work, the WB limit is closer to current cosmic rays and neutrino production models. The opaque sources are in the “hidden” sources category.

2.1.3. “Hidden” Sources

The energy spectrum from opaque sources is not constrained by the observed cosmic ray flux (see section 2.1.1). Therefore models which predict such spectra are not limited by the WB derivation nor by the MPR for “thin” sources. These models assume sources that are “optically thick” to nucleons. The nucleons must first be accelerated to high energies and then encounter a target (radiation or matter) abundant enough to interact with most of the protons but low enough that the pions and muons are able to propagate freely and decay and then the neutrinos be allowed to escape. Berezhinsky and Dokuchaev (Berezhinsky and Dokuchaev 2001) have proposed such a model and find that such a source could produce up to 10 muons crossing a one square kilometer area per year. One could argue that such a high flux would be limited to a short term (10 years out of billions) outburst. However, the long term limit for all sources is close to the WB limit.

Another model that assumes a source which is “optically thick” to nucleons has been proposed by Stecker et al (Stecker et al. 1991 and 1992). It proposes that protons are accelerated to high energies in the AGN core. These protons produce neutrinos through photo-meson production. This model will however be constrained by the MPR “opaque” limit since the production of neutrinos must be accompanied by gamma production. Such sources should also produce lower energy neutrinos and these are not seen by current experiments (Barwick 2001).

A way to avoid both the WB and MPR limits is the production of neutrinos in a way other than the photo-meson or proton-nucleon interactions. There is a vast list of models that can account for this possibility. A list of them can be found in (Bahcall and Waxman 1999). Most of these involve new or “exotic” physics and we do not include them as “astrophysical” sources.

As discussed in section 2.1.2, neutrino fluxes from hidden sources are less likely to be produced.

2.1.4. *GZK Fluxes*

Very high-energy protons traveling through intergalactic space interact with the cosmic background photons and photo-produce pions. Greisen and Zatsepin and Kuz'min (Greisen 1966 and Zatsepin and Kuzmin 1966) first pointed out that this process would occur and that it would set an upper bound to the maximum energy (a few times 10^{19} GeV) for a proton traveling intergalactic distances (hundreds Mpc).

The production and flux of high energy neutrinos originated from intergalactic propagation of ultra high energy cosmic rays has been determined in (Engle and Stanev 2001). They assume that the ultra-high energy cosmic rays are of astrophysical origin and show their result for different assumptions on cosmic ray source distributions, injection spectra and cosmological evolution. Their results with the same assumption for the injection power and cosmological evolution as Waxman and Bahcall (Waxman and Bahcall 1999) are shown in Figure 3.

2.1.5. *Neutrinos from the Galaxy*

There is a significant diffuse flux of neutrinos created by interactions of the galactic and extra-galactic cosmic rays with interstellar matter and starlight. The spectrum of cosmic rays is reasonably well known, as is the distribution of targets in our Galaxy. We call the flux of neutrinos created by interactions in the interstellar medium the “galactic flux”.

Estimates of the galactic neutrino flux have been made by Domokos (Domokos 1993), Berezhinsky et al. (Berezhinsky et al 1993), and Ingleman and Thunman (Ingleman and Thunman 1996). The diffuse galactic neutrino flux can be separated from the local atmospheric neutrino flux at energies above 10^{15} eV.

Above these energies the flux of diffuse galactic neutrinos stays harder than the atmospheric flux both because the original galactic cosmic rays have a harder spectrum nearer the center of the galaxy and most important the interstellar material is sufficiently thin and far away that the muons have adequate range and time to decay.

The muon neutrino flux (per GeV cm² sr s) is estimated (Ingleman and Thunman 1996) by

$$\phi_\nu = \begin{cases} 3.0 \times 10^{-6} RE^{-2.63} & E_\nu < 4.7 \times 10^5 \text{ GeV} \\ 1.9 \times 10^{-4} RE^{-2.95} & E_\nu > 4.7 \times 10^5 \text{ GeV} \end{cases} \quad (3)$$

where R is the distance to the edge of the galaxy in Kpc.

The resulting flux from the direction of the center of the galaxy (20.5 kpc) and from the direction orthogonal to the galactic plane (0.26 kpc) are shown in Figure 2. Both the WB and MPR limits are for extra-galactic neutrinos.

One important point when considering the galactic flux is the direction from which the neutrinos come. Experiments in the South Pole will not detect fully the neutrinos from the center of the galaxy. This flux can be well measured by experiments in the northern hemisphere.

2.2. Point Sources

In this section we consider sources that produce high-energy particles. Other than the hidden sources mentioned in section 2.1.3 active galactic nuclei and gamma-ray bursters are examples of these sources. In principle a sufficiently bright point source can have their locations determined by the arrival direction of these particles (or by the particles produced by them) at the detector. The relevant issue is that, if the location of the source is pre-known, then the effective atmospheric background is effectively reduced by the ratio of the effective solid angles. The intrinsic angular deviation between the neutrino and daughter muon is of order $0.7^\circ/\sqrt{E_\nu/\text{TeV}}$ (Gaisser 1990) so that the effective solid angle is of order one square degree. If the detector angular resolution is of this order, then the relative enhancement of signal-to-background can be as much as 10^4 .

2.2.1. Active Galactic Nuclei

Active Galactic Nuclei (AGN) are one of the brightest known astrophysical sources. They produce a multi-wavelength spectrum that goes from radio to TeV gamma rays. How such high-energy gammas are produced is still to be fully understood.

In the more conventional model high energy photons are produced by inverse Compton scattering of accelerated electrons on thermal UV photons (Sikora Begelman and Rees 1994). This description is supported by multi-wavelength observations of Mkn 421 (Macomb et al 1995 1996) although there are adjustments to be made (Halzen and Zas 1997).

Other models (Mannheim 1995; Halzen and Zas 1997; Protheroe 1996) describe the production of high energy gamma rays through the decay of photo produced neutral pions. These protons would be produced and accelerated in the AGN jet. This mechanism would be responsible for the production of the observed gamma-ray background.

Figure 4 shows that the non conventional model (Mannheim 1995; Halzen and Zas 1997; Protheroe 1996) predictions are much higher than the WB limit. Waxman and Bahcall (Bahcall and Waxman 1999) show that the sources in these models are optically thin and therefore should be constrained by their limit. They conclude that one of the basic assumptions of these models has to be wrong.

It is important to note that the AGN sources are intermittent and that they might violate the WB limit in a temporary basis. However they should not do so when averaged over time.

2.2.2. Gamma-ray bursts

Energetic gamma-ray bursts (GRB) seem to be successfully explained by fireball models ((Piran 1994) and references therein). Recent observations suggest that they originate in cosmological sources. Waxman and Bahcall (Waxman and Bahcall 1997) propose that neutrinos are a consequence of these fireballs. They will be produced by photo-meson production between the fireball gamma-rays and accelerated protons. (Waxman and Bahcall 1997; Waxman and Bahcall 1999) derive the energy spectrum and flux of high energy neutrinos created in this way. Their result is in agreement with (Rachen and Meszaros 1998).

Figure 4 shows the predicted spectrum of high energy neutrinos from GRBs. This spectrum is consistent with the WB limit and the intensity over 2π sr coverage would be about 10 neutrino induced muons per year (Waxman and Bahcall 1999). These neutrinos have the advantage of spatial and temporal coincidence with GRB photons which can be used as a tool to reduce the atmospheric neutrino background. The neutrinos produced from hadronic interaction may arrive on a time scale of about an hour after the photons in the model of simple acceleration (Waxman and Loeb 2001).

2.2.3. Neutrinos from the Sun

There are a number of estimates of the flux of high-energy neutrinos produced by cosmic rays interacting in the Solar atmosphere . They typically predict tens of neutrinos per square kilometer per year from the solid angle of the Sun (Hettlage et al. 2000).

2.3. Atmospheric Neutrino Fluxes

The atmospheric neutrino flux is the main background for neutrinos from astrophysical sources. As a parameterization of this background flux we use the derivation made by Volkova (Volkova 1980).

Volkova derives the atmospheric neutrino flux from the decay of light mesons (K, π) and muons and from the decay of short-lived particles (prompt decay) which mainly includes charm particles. The latter will only be significant at higher energies (above a PeV).

Figures 5 and 6 (extracted from (Albuquerque and Smoot 2001)) show the total vertical and horizontal atmospheric neutrino flux including the contributions from mesons and muons and from prompt decays.

We compare this flux with that obtained by (Honda et al 1995) and (Agrawal et al. 1996). The biggest difference between these calculations is of about 15% (see Figure 14 of ref. (Honda et al 1995) and Figure 7 of ref. (Agrawal et al. 1996)). In the energy range of interest to our work, the discrepancy is less than 15% and the Volkova spectrum is underestimated in relation to these other spectra.

Since the atmospheric neutrino flux is almost irreducible, understanding the effect of its uncertainty is important. The uncertainties come from the primary cosmic ray flux measurement and from the inclusive cross section for proton – nucleon interactions. We assume the biggest discrepancy between the atmospheric flux calculations (15%) as the uncertainty in the magnitude of the atmospheric flux.

Since the uncertainty in the primary spectrum increases with energy there is also an uncertainty in the slope of the spectrum. At lower energy there are more data and the uncertainty is mainly due to instrumental efficiency and exposure factor. At higher energies the uncertainty is dominated by limited statistics. In general (Honda et al 1995; Agrawal et al. 1996) the uncertainty in the spectrum slope is assumed to be about 10% below 3 GeV increasing to 20% at 3×10^3 GeV and remaining constant from thereon. As discussed also in (Honda et al 1995; Agrawal et al. 1996) the uncertainties in the interaction model at higher energies is estimated around 10%. Neutrino oscillations do not affect the atmospheric spectrum at the energies of interest here.

One can therefore estimate the overall uncertainty in the atmospheric neutrino flux as around 20%. We will show that this uncertainty does not affect significantly our results.

Although the atmospheric neutrino flux is always considered as a background for neutrino astrophysics, the fact that the flux at higher energies is not well determined by experiments, makes it an important measurement to be performed with neutrino telescopes. It

has been suggested that the standard model neutrino cross section above 10^8 GeV might be lower than expected (Dicus et al. 2001). Measuring the atmospheric neutrino flux at these energies can determine the neutrino – nucleon cross section (Kusenko and Weiler 2001). It is important to note that these energies cannot be directly probed by accelerator experiments.

2.4. Summary of Fluxes

Figure 7 shows a summary of the expected fluxes arriving at the surface of the Earth. The atmospheric background dominates at low energy. Neutrinos from the center of the galaxy contribute a small excess to the atmospheric flux at energies above 10^6 GeV, but are constrained by a smaller solid angle. They are not in the field of view of South Pole detectors, but are interesting for more equatorial detectors. Diffuse limits on astrophysical neutrinos are characterized by the WB limit. The WB limit is avoided by the MPR limits as they abandon the power-spectrum for optically thin limit and propose “hidden” source contributions for the optically thick limit. GZK fluxes are shown at the highest energies. The most promising flux to be measured is the one from GRBs since it allows reduction of the background through knowledge of arrival time and direction.

Detected event rates are smaller since the neutrino conversion into a muon and the efficiency of the detector have to be taken into account. Event rates and experimental sensitivity are considered in the next section.

A sensible design criteria for a neutrino detector is that it be sensitive to the highest known neutrino flux from astrophysical sources, namely five times below the WB limit. With such a sensitivity, backgrounds can be characterized and new diffuse fluxes discovered. Physics measurements of the new fluxes, namely brightness, energy spectrum and points on the sky, will require substantially more events.

3. Event Rates and Sensitivity

Neutrinos cannot be directly detected, because they do not deposit a significant amount of energy as they pass through matter. For a neutrino to be observed it must undergo an electro-weak interaction with another particle resulting in detectable secondaries. Since the neutrino interaction cross section is small, the probability of an interaction can be increased if large, dense targets are used, such as the Earth.

The neutrino nucleon cross section increases as a function of energy resulting in two effects. First, high energy neutrinos are more likely to interact within the detector volume.

Second, the flux of neutrinos that reach the detector is attenuated at high energy because of neutrino interactions in the Earth. High energy muons travel many kilometers before stopping or decaying. The advantage of detecting muons is that the detector could be sensitive to neutrino interactions over a length equal to the muon range. Unfortunately, because high-energy muons lose energy rapidly and because at low energy there is a large atmospherically-produced neutrino background, this potential gain is reduced.

Convolution of the neutrino flux, conversion cross sections, muon range and deposited energy is the subject of the next sections.

3.1. Neutrino Interactions

The flux of leptons converted from the incident neutrino flux is

$$\phi_{lepton} = \phi_{\nu} P(\nu \rightarrow lepton) \quad (4)$$

where $P(\nu \rightarrow lepton)$ is the probability that a neutrino suffers an interaction and produces a lepton. This probability is given by

$$P_I = P(\nu \rightarrow lepton) = \int_0^{path} n \sigma(\nu \rightarrow lepton) dx \quad (5)$$

where n is the nucleon number density and σ is the neutrino nucleon cross section and the path is the distance the neutrino traveled. In the following, we abbreviate the notation: $P_I = n \sigma_{\nu} L$ where L is the neutrino path.

The deep inelastic neutrino cross sections, σ_{ν} are determined using CTEQ4-DIS parton distribution functions as described in (Gandhi et al. 1998). Cross sections with electron targets are smaller by at least an order of magnitude, except for near the W resonance, where electron neutrinos interact very strongly. In the case of muon neutrinos, the interaction probability is dominated by the charge current (CC) cross section, but there is also some degradation of neutrino energy by the neutral current (NC) cross section.

Neutrino fluxes will suffer attenuation as they pass through the Earth. The differential flux is given by

$$\frac{d\phi_{\nu}}{dx} = -n \sigma_{\nu} \phi_{\nu} \quad (6)$$

where x is the distance traveled by the neutrino. Integrating over the path length traversed by the neutrino, we find

$$\phi_{\nu} = \phi_{\nu 0} e^{-\int n \sigma(\nu) dx} = \phi_{\nu 0} P_S \quad (7)$$

where $\phi_{\nu 0}$ is the flux at the earth’s surface, P_S is the survival probability and the argument of the exponential term is P_I integrated over all cross sections that make the neutrino cease to exist.

Figure 8 shows the muon neutrino survival probability at a point on the surface of the earth for a variety of neutrino energies as a function of the cosine of the earth angle, θ_Z ¹. The number density (see Equation 5) is determined by an integration of the earth density profile which is taken from (Gandhi et al. 1996; Dziewonski 1989). The upper lines are the probability using only CC interactions. The lower lines include both CC and NC interactions. It shows that the NC interaction will decrease the lepton flux by about 10%. At high energy, the steep cut-off results in as much as a 20% decrease. The NC interaction does not actually remove the neutrino from the flux, but degrades its energy. We include it in our analysis to be conservative, and treat the CC-only case as an upper bound to the systematic uncertainty.

From Figure 8 one can see that the survival probability becomes quite small for high energy neutrinos due to significant attenuation. At low energies, the attenuation is negligible, but it begins to contribute above about 10 TeV. The Earth becomes essentially opaque to neutrinos at energies of above a PeV (Gandhi et al. 1998).

The effect of the dense Earth core can be seen near $\cos \theta_Z$ of 0.8. Neutrinos that travel close to the Earth axis will go through most of the Earth core and therefore increase their probability of interaction. There is also evidence of a thin crust in the model at small $\cos \theta_Z$ where neutrinos only pass through the crust.

The flux of muons interacting in a detector volume is given by

$$\phi_{lepton} = \phi_{\nu 0} \times P_S \times P_I \quad (8)$$

where the incident flux, $\phi_{\nu 0}$, is the flux in Figure 7 and P_I is now integrated over the neutrino path through the detector.

¹ θ_Z is the angle from local zenith. An upward going neutrino, that is, one coming from the direction of the center of the Earth as viewed from the detector has a zenith angle of zero degrees.

3.2. Muon Fluxes

Muons will propagate, losing energy until they eventually come to rest and decay or undergo a nuclear reaction. The mean energy loss is given by

$$\frac{dE_\mu}{dx} = a + bE_\mu \quad (9)$$

where asymptotically $a = 2 \times 10^{-3} \text{GeVcm}^2/\text{g}$ and $b = 4 \times 10^{-6} \text{cm}^2/\text{g}$ (D.E. Groom et al. 2000a) are respectively ionization and radiation loss parameters.

Approximating the parameters $a(E_\mu)$ and $b(E_\mu)$ as constants, simple integration over the muon path yields the muon range, R_μ .

$$R_\mu = \frac{1}{b} \ln \left(1 + \frac{b}{a} E_0 \right) \quad (10)$$

where E_0 is the muon initial energy. Below the critical energy² ionization losses dominate and the muon range is well described by the average energy loss. At high energies where radiative processes dominate, large fluctuations develop and a stochastic approach is needed. The mean muon range is shorter than Equation 10 would suggest. Lipari and Stanev (Lipari and Stanev 1991) developed a Monte Carlo with the purpose of taking these fluctuations into account. We use their Monte Carlo to determine the muon range. This approach also accounts for the energy dependence of the energy loss parameters a and b .

We now determine the muon rate in an idealized detector located 1.5 km below the surface of the earth with a detector path length of 1 km for all incident angles. Two muon rates are relevant, those where the muon is produced inside the detector (P_I integrated over 1 km) and those where the muon originates outside the detector and ranges into the detector (P_I integrated over the muon range). Figure 9 shows the upward flux of muons plus anti-muons versus neutrino energy for the WB limit, the MPR limit, GRB flux, GZK flux, and for atmospheric neutrinos. Only muons with more than 100 GeV are included. These results are in good agreement with (Gaisser 2000). The lower curve is the flux of muons plus anti-muons that start outside the detector volume and range into it. The upper curve includes the flux of muons and anti-muons that start in the detector volume. Except for very low energies, the dominant flux is from muons that range into the detector.

Muon rates are substantially lower than the neutrino rates shown earlier. The line on Figure 9 shows where 1 event/year is expected for each half decade in energy. The GZK flux

²Critical energy is the one for which the probability for a nuclear interaction in one nuclear mean free path equals the decay probability in the same path. It is given by $E_{critical} \equiv \frac{b}{a}$.

peaks at 10^9 GeV, just below the WB limit. About 0.17 muon per year is expected from the GZK flux.

For all but the atmospheric flux, equal numbers of neutrinos and anti-neutrinos are expected. Atmospheric neutrinos exceed anti-neutrinos by a factor of 2.5 at 1 TeV (Agrawal et al. 1996). By about 100 TeV, however, the neutrino and anti-neutrino cross sections become equal. Across the whole spectrum, the uncertainty due to muon/anti-muon composition can be neglected since it is smaller than the theoretical uncertainty of $\pm 20\%$.

Since the neutrino energy is not measured by the detector, but rather the muon energy is estimated by energy deposition in the detector, the results are better shown as a function of the muon energy estimation. The latter can be achieved in three steps: (1) first the flux in muon energy, (2) flux in muon energy at the detector, and (3) finally flux as a function of the energy deposition in the detector. The muon flux as a function of muon energy is given by

$$\phi_\mu = \int_0^\infty \frac{d}{dE_\mu} \left(\frac{d\phi_\nu}{dE_\nu} \right) dE_\nu \quad (11)$$

Figure 10 shows the muon and anti-muon flux resulting from neutrinos as a function of initial muon energy.

The average energy loss in a CC interaction, $y = (1 - E_\mu/E_\nu)$, for neutrinos energies between 10 GeV and 100 GeV is 0.48 gradually decreasing to about 0.2 at high energies (Gandhi et al. 1996). At high energy, the muon gets about 80% of the neutrino energy. A comparison between Figure 9 and Figure 10 shows that the flux is shifted on the muon energy scale by just this factor.

A stronger effect is noticed if we determine the flux as a function of the muon energy as it enters the detector. A very high-energy neutrino will make a very high-energy muon that travels many kilometers losing energy as it goes. If the track starts at random distance from the detector, the measured energy will be distributed nearly uniformly between the initial energy and zero. A high-energy muon will lose on average $1-1/e$ of its energy when traversing between 2.4 and 3 km of ice. About each 2.7 km of ice traversed will move the muon down a natural logarithmic energy interval of muon energy at the detector. We use the Lipari-Stanev Monte-Carlo (Lipari and Stanev 1991) to determine the muon range and the energy deposited in 100 m steps including fluctuations from radiative processes. A random spot is chosen along the track to represent the point it enters the detector. Figure 11 shows the muon plus anti-muon flux resulting from neutrino interactions as a function of the muon energy as it enters the detector.

The atmospheric neutrino flux is a major background over most of the energy range where events can be measured in a km^2 per year. To detect the high-energy signals, good

energy resolution is needed. For point sources, the muon energy is used as a cut parameter to optimize signal to background. For the diffuse flux, the resolution is needed to deconvolve the spectrum back to the neutrino energy. Where signals are not detected, a cut on muon energy is needed to set upper limits.

3.3. Muon Energy Resolution

Muon energies below about 100 GeV are measured by their path length. At higher energies, the path lengths become too long and the Cherenkov radiation from the track is used. The total Cherenkov radiation is nearly proportional to the total energy deposition in the detector volume. Figure 12 shows the deposited energy in MeV/m for 100, 500 and 1000 meter track lengths at a variety of muon energies. The distribution is essentially a Gaussian with a long tail to larger energy deposition due to the stochastic nature of the energy loss processes³. The energy loss includes (Lipari and Stanev 1991) the usual ionization and knock-on electron processes important at lower energies and additional processes important at higher energies including pair production ($\propto \Delta E^{-2}$), bremsstrahlung ($\propto \Delta E^{-1}$), and photonuclear (roughly $\propto \Delta E^{-1.1}$), all with a cut off at the total energy of the muon. These processes are responsible for the energy dependent portion of dE/dx . The numerous lower energy pairs (plus ionization) produce ⁴ the Gaussian-peaked shape for most energy losses. The bremsstrahlung and photonuclear processes and the rarer high-energy pairs produce a significant tail of much larger energy depositions. If the most probable (or mean) energy deposition is used as a measure of the muon energy, a significant number of the much more abundant lower energy muons will be reconstructed as high energy muons. As a result a significant number of the abundant atmospheric muons would be reconstructed as much higher energy muons. Longer sampling path lengths have a more truncated tail because there is a cut off where the muon is completely stopped. The deposited energy can not

³The energy losses determined by the Lipari-Stanev Monte Carlo and more modern codes (Chirkin and Rhode) are represented by a delta function and a radiative tail. Depending on the energy, there will be a gap between these two parts (larger tracks have less gap). We make a smooth parameterization to avoid this gap. We use the difference between the Lipari-Stanev standard prediction and our parameterizations as an estimate of the systematic uncertainty inherent in all currently available calculations.

⁴The Central Limit Theorem states that the probability distribution of sum of variables drawn from probability distributions with finite variances will tend towards the normal (Gaussian) distribution. The very numerous low-energy deposition processes will result in a nearly Gaussian peaked shape around the most probable energy loss for most energy depositions. The much rarer high-energy losses take many more samples to average down and result in a long tail to higher-energy deposition. A true $1/\Delta E$ distribution would not tend to Gaussian as it has an infinite variance were it not for the maximum energy cut-off.

exceed the muon energy. A clear statistical relationship exists between detected and true muon energy.

An ideal detector could measure the deposited energy perfectly. If an ideal detector made many measurements with independent 100 meter samples, then events that fluctuated early could be removed at the expense of efficiency and the true muon energy could be measured using the samples up to the first large fluctuation. The Frejus detector (Rhode et al 1996) being a sampling calorimeter determined the muon energy based on fluctuations in energy deposition. The large scale of more recent neutrino detectors makes independent sampling unrealistic. In an open geometry, such as Cherenkov detectors, the samples can not be cleanly separated with opaque barriers. Long path lengths are an advantage because they minimize the sensitivity to the long tails in the energy resolution. Under sampling can reduce the advantage of long path lengths, however if the detector is only able to measure portions of the energy deposition. Figure 13 shows the muon flux as a function of energy deposited in the detector as radiation in a 500 meter track.

Figure 14 is included to show the main systematic effects on the spectrum. High energy muons are most sensitive to the NC effect on survival probability. The shape of the atmospheric background depends more significantly on the length of the track. In addition to the systematics shown on the plot, there is about 20% theoretical uncertainty in the predicted atmospheric flux (see section 2.3).

3.4. Sensitivity of an Ideal km^2 Detector to Astrophysical Sources

Event rates above a cut where signal and background are equal are listed in Table 1. Also included are rates for two other possible energy cuts: the energy where no background events are expected (atmospheric < 0.1 event), and the energy where 1 background event is expected. Uncertainties in the rates come from several sources. There is a theoretical uncertainty on the atmospheric background of $\pm 20\%$. The NC contribution to the survival probability is $+10\%$. Finally, the difference between Lipari-Stanev and a smooth parameterization of the energy deposition adds $\pm 10\%$ for 500 meter tracks and $\pm 50\%$ for 100 meter tracks. The total uncertainties in the event rates quoted (500 m tracks) are: $+14\%$, -10% for signals and $+24\%$, -22% for the atmospheric flux.

Also included in the table are a series of sources consistent with the MPR optically thin limit. Since this limit is not a power law, it implies that individual sources would make up the distribution. The maximum power-law spectrum consistent at all energies is the WB limit. Figure 15 shows the neutrino flux for these made-up sources. We generously give them

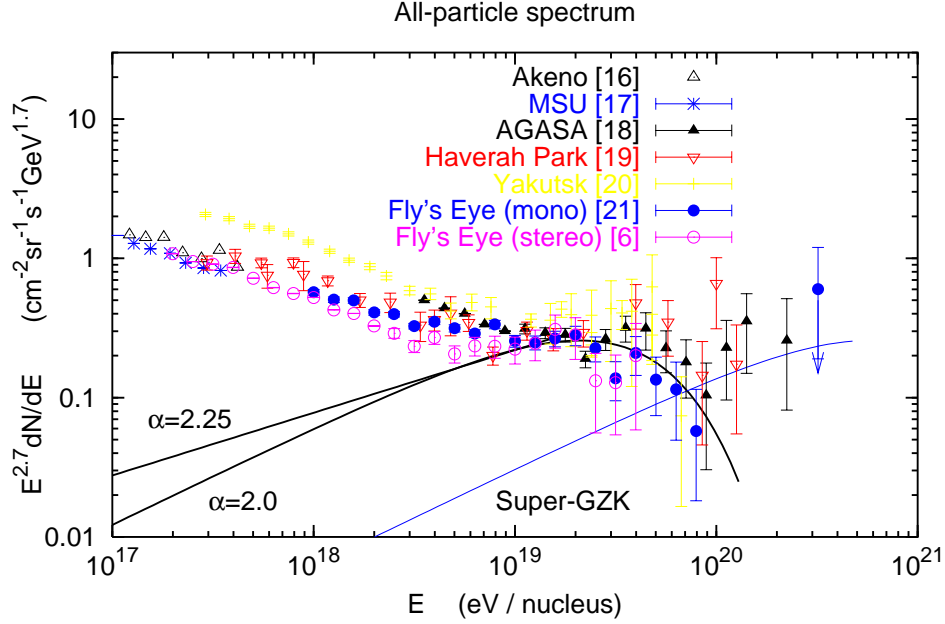


Fig. 1.— Cosmic Ray flux versus cosmic ray energy (extracted from (Gaisser 2000)). Fits for two cosmic ray spectral indices (α) are shown.

Muon Source	events	events	energy (Mev/m)	events
	$E > 10^{5.5}$ MeV/m	$E > 10^{4.95}$ MeV/m	$S/B=1$	$E > S/B=1$
Atmospheric Neutrinos	0.11	1		
WB Opt Thin Limit	3.0	7.8	$10^{4.3}$	23.8
MPR Opt Thin Limit	15.5	90.0	$10^{2.8}$	7500.0
MPR Opaque Limit	112.0	300.0	$10^{2.9}$	7050.0
MPR Source (3 GeV)	10^{-12}	10^{-7}		
MPR Source (4 GeV)	0.0003	0.31	$10^{3.0}$	2500.0
MPR Source (5 GeV)	3.4	60.0	$10^{2.9}$	4000.0
MPR Source (6 GeV)	5.8	21.0	$10^{3.9}$	76.0
MPR Source (7 GeV)	2.5	4.5	$10^{4.5}$	6.4
MPR Source (8 GeV)	0.9	1.3	$10^{4.9}$	1.4
MPR Source (11 GeV)	0.1	0.1		

Table 1: Event rates for 500 meter long muon tracks in an ideal km^2 detector. The background is composed of atmospheric neutrinos. Background-free limits can be estimated for deposited energy $> 10^{5.5}$ MeV/m. A single background event is expected for energy $> 10^{4.95}$ MeV/m. Finally, the energy and rates where the signal equals background ($S/B=1$) are listed. Uncertainties in event rates are +24%, -22% for atmospheric background and +14%, -10% for the other signals.

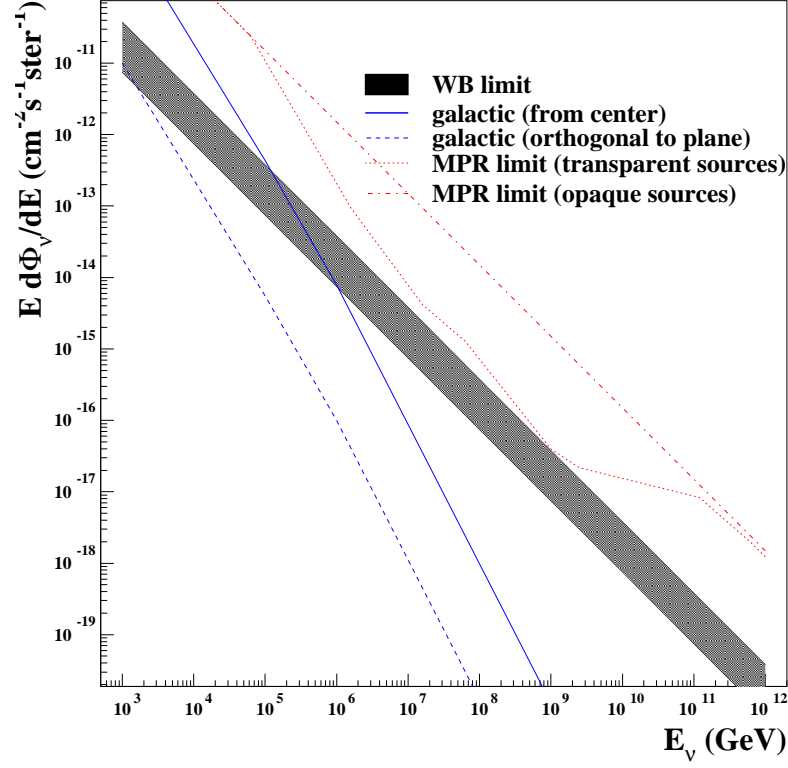


Fig. 2.— Neutrino fluxes from astrophysical sources and upper bound on the total diffuse neutrino flux. The lower edge of the shaded area is the WB limit (Waxman and Bahcall 1999) with no cosmological evolution, the upper edge is the same limit taking evolution into account. The dashed line is the MPR (Mannheim Protheroe and Rachen 2001) limit for transparent sources and the dotted dashed line for opaque sources. The continuous line is the flux from the Galactic center and the dashed line is the galactic flux from the direction orthogonal to the galactic plane (Ingleman and Thunman 1996).

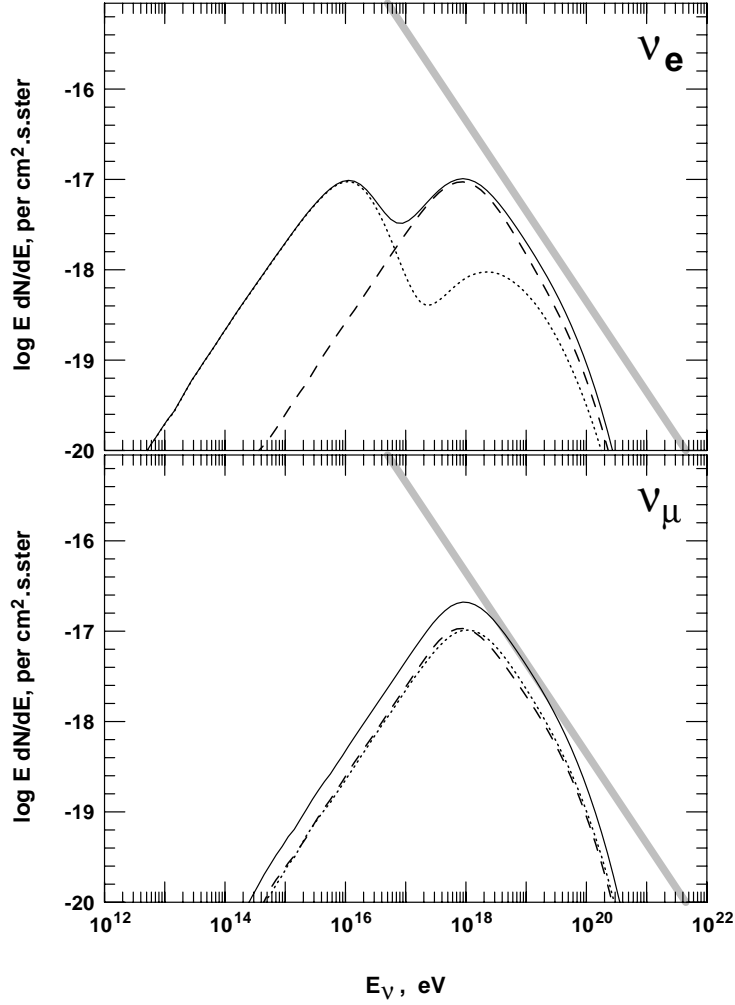


Fig. 3.— Fluxes of neutrinos generated by ultra high energy protons. Fluxes of electron neutrinos (dashed lines) and anti-neutrinos (dotted lines) are shown in the upper panel. The lower panel shows the fluxes of muon neutrinos and anti-neutrinos. Solid lines show the sum of neutrinos and anti-neutrinos. These fluxes were calculated in (Engle and Stanev 2001) using the same injection power and cosmological source evolution as the WB limit (Waxman and Bahcall 1999). This limit is represented by the shaded line. Figure extracted from (Engle and Stanev 2001).

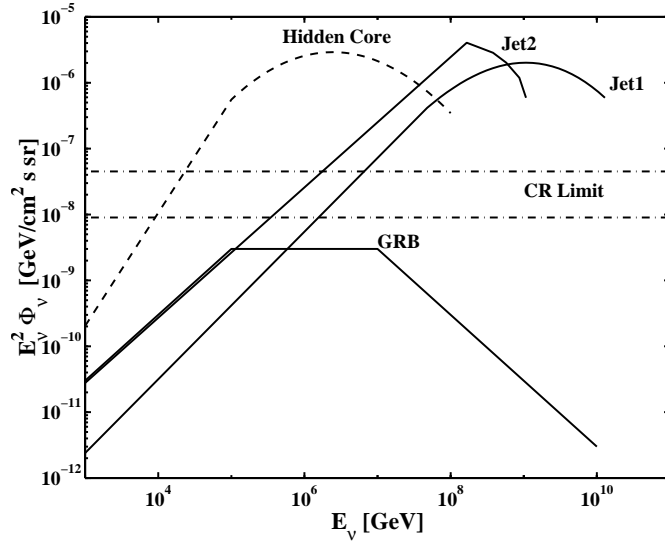


Fig. 4.— Muon neutrino flux weighted by muon neutrino energy versus muon neutrino energy. The WB limit is labeled as CR limit and compared to theoretical models. The Jet1 models refers to results from (Mannheim 1995) and Jet2 from (Halzen and Zas 1997). These models should be constrained by the WB limit. As they violate the limit, WB conclude that one of their assumptions must be wrong. The GRB model is a prediction for neutrinos from Gamma Ray Bursts (Waxman and Bahcall 1999; Waxman and Bahcall 1997). The WB limit is also compared to a hidden source model (Stecker et al. 1991 and 1992) for which the WB limit does not apply (see section 2.1.3). This model is partially ruled out by the AMANDA published limit (Barwick 2001). Figure extracted from (Waxman and Bahcall 1999).

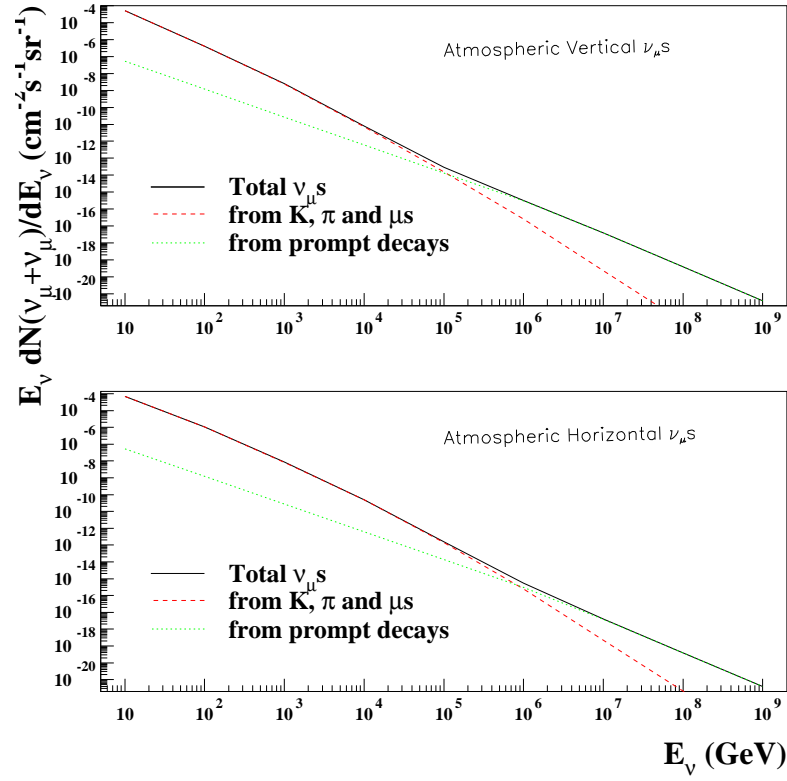


Fig. 5.— Atmospheric vertical and horizontal (as labeled) muon neutrino energy spectra based on (Volkova 1980). Also the contribution from K , π and μ 's and from prompt decays.

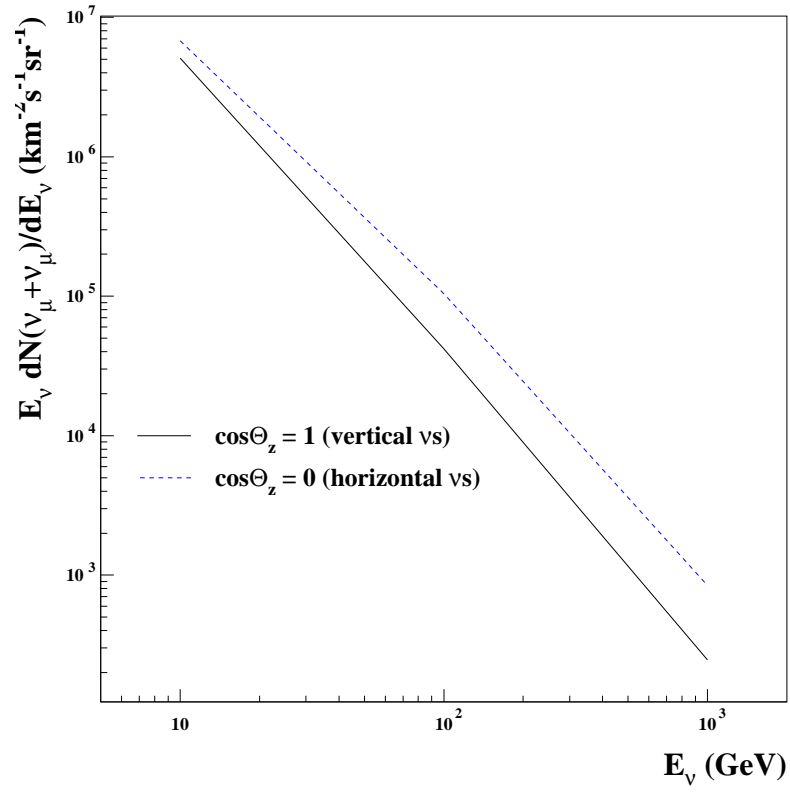


Fig. 6.— Atmospheric vertical and horizontal (as labeled) muon neutrino energy spectra. Note that it is plotted per km^2 instead of cm^2 as in the previous figure. The flux of horizontal neutrinos is bigger than vertically down going neutrinos since the muons have more opportunity to decay.

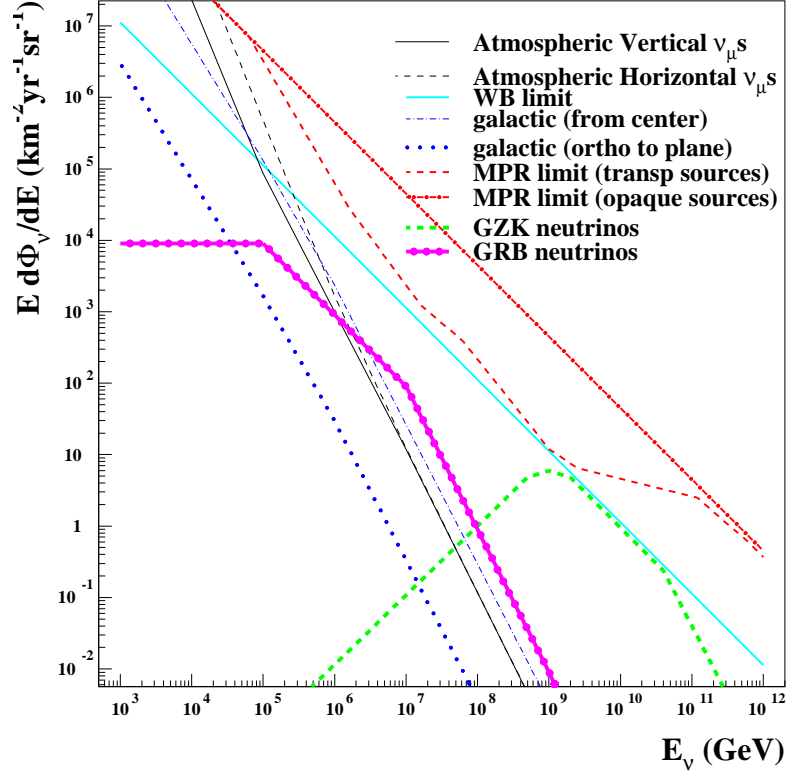


Fig. 7.— Neutrino Fluxes summary containing (1) Atmospheric vertical (solid line) and horizontal (dashed) muon neutrino energy spectra based on (Volkova 1980). The reason why these two fluxes overlap at high energies (above 10^6 GeV) is that prompt decays (mainly from charm particles) dominate the atmospheric flux when compared to meson and muon decay at these energies. (2) WB (Waxman and Bahcall 1999) limit (with evolution) for neutrino fluxes from astrophysical sources (large solid line). (3) Galactic neutrino flux (Ingleman and Thunman 1996) from galactic center (dotted dashed line) and from direction orthogonal to the galactic plane (dotted). (4) MPR (Mannheim Protheroe and Rachen 2001) limit for neutrino fluxes from sources transparent to nucleons (medium dashed line) and from sources opaque to nucleons (medium dotted dashed). (5) Estimate of GZK neutrinos (Engle and Stanev 2001) (large dashed line). (6) Estimate of GRB neutrinos (Waxman and Bahcall 1997) (large dot dashed line).

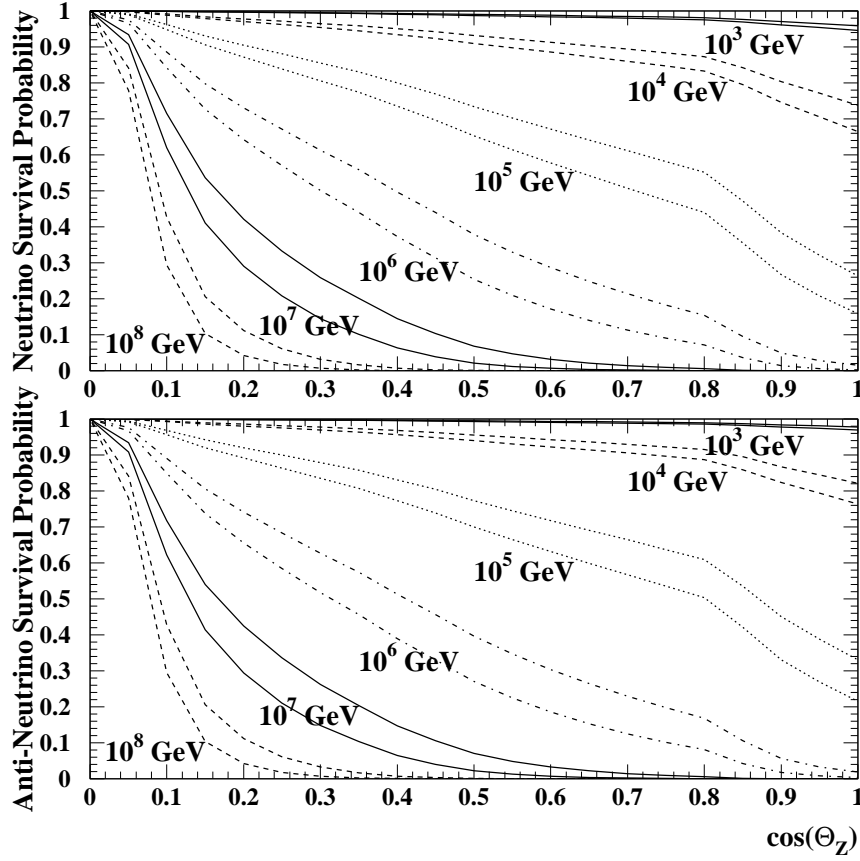


Fig. 8.— Survival probability for neutrinos and anti-neutrinos transversing the Earth as a function of $\cos(\theta_Z)$. The horizon is at 0, and a path through the center of the earth is at 1. The upper lines include only CC interactions, the lower lines include both CC and NC interactions. Differences due to NC interactions have a maximum effect at high energy where the distributions drop sharply.

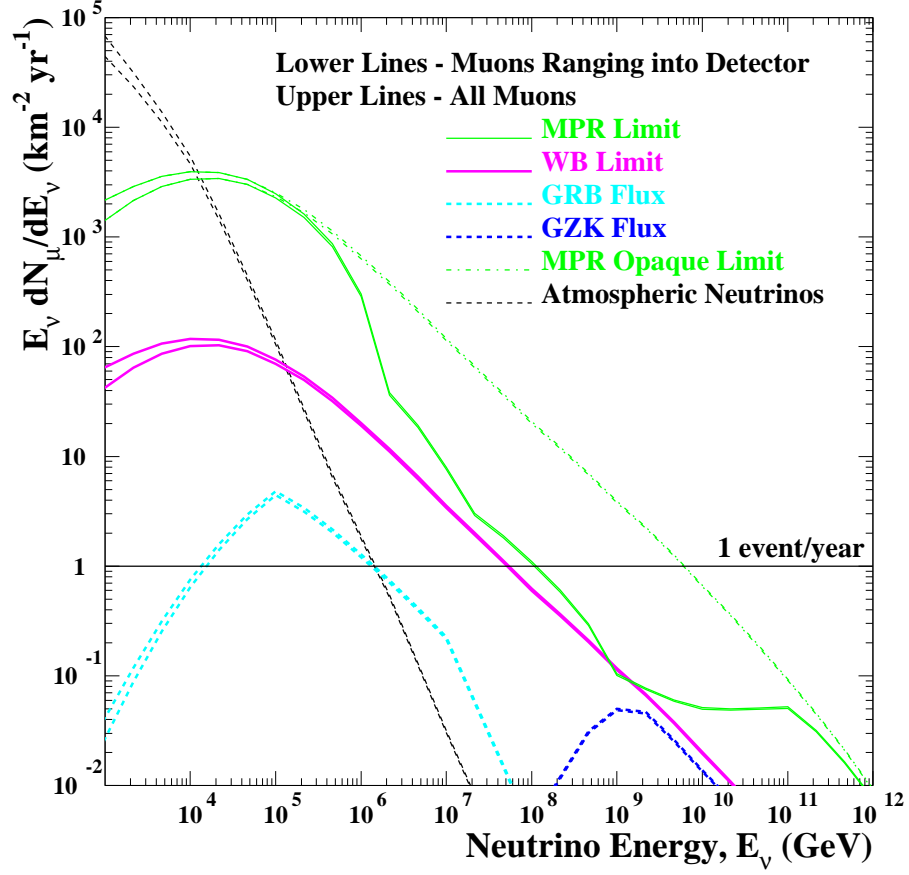


Fig. 9.— Muon and anti-muon flux as a function of neutrino energy. Most muons range into the detector although the fraction starting inside increases at low energy.

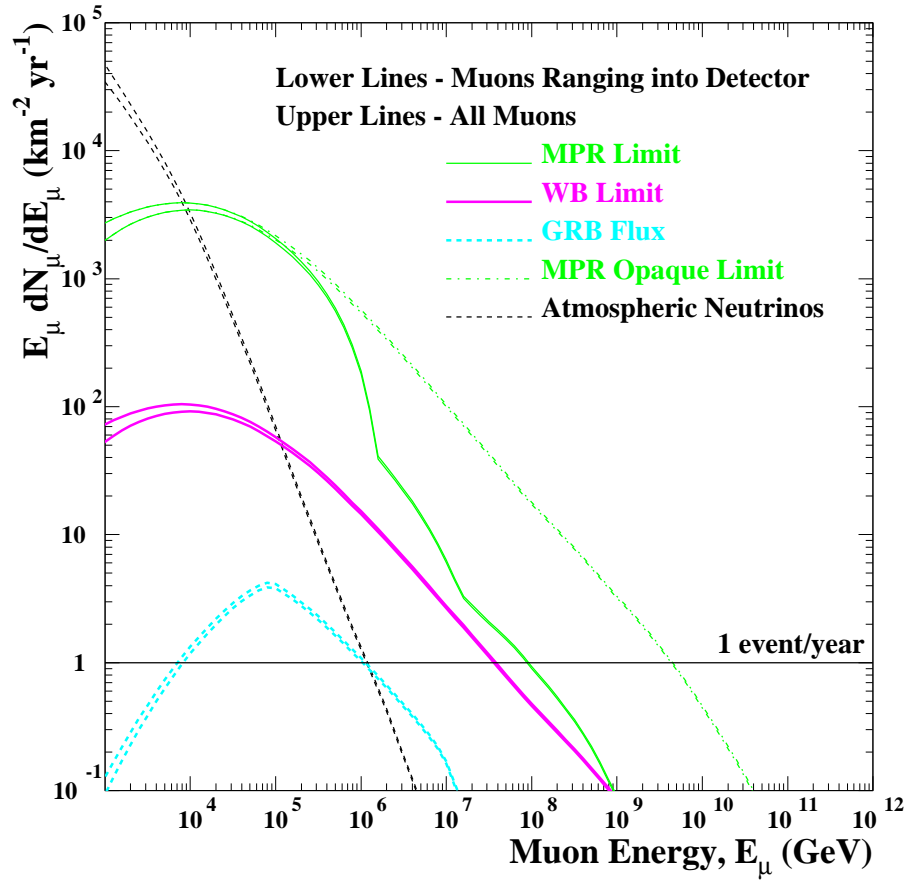


Fig. 10.— Muon and anti-muon flux as a function of the initial muon energy.

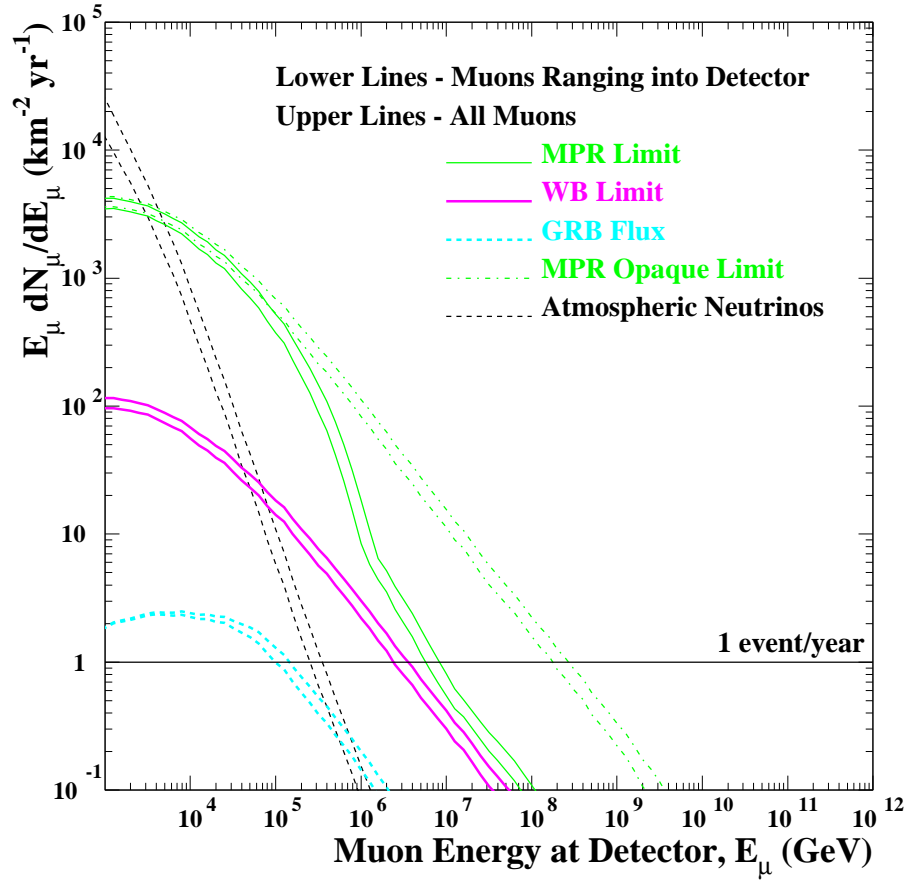


Fig. 11.— Muon and anti-muon flux as a function of the muon energy when it enters the detector. The measured energy of muons that range into the detector is less than the initial energy. Muons that start inside the detector make up about 30% of the flux at high energy.

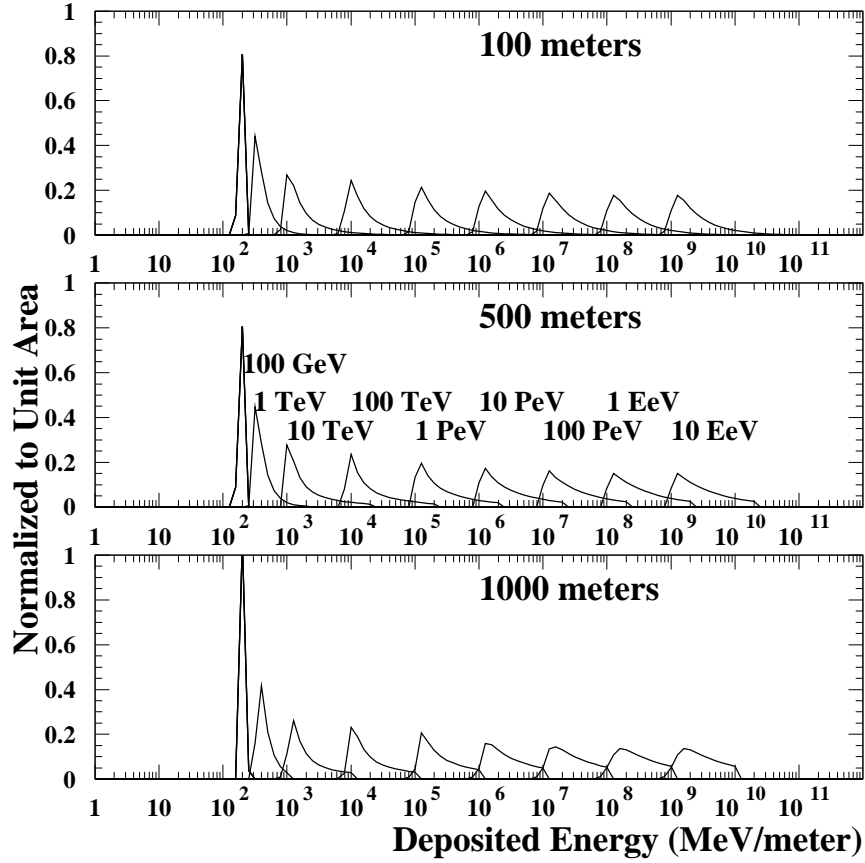


Fig. 12.— Energy deposited in MeV/m for 100m, 500m, and 1 km muon paths. Notice there is a strong dependence in the deposited energy on the true muon energy until the muon energy drops below about 100 GeV.

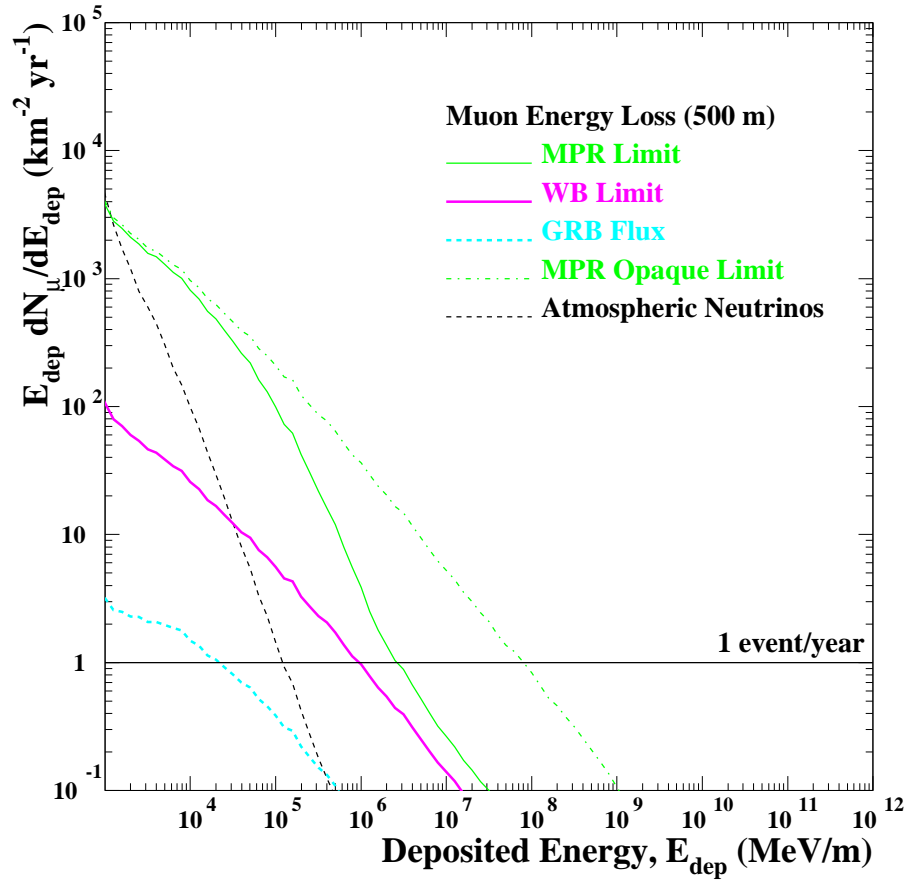


Fig. 13.— Muon and anti-muon flux as a function of the energy deposited in the detector. The muon flux is peaked at minimum ionizing energy, with a tail to high energy.

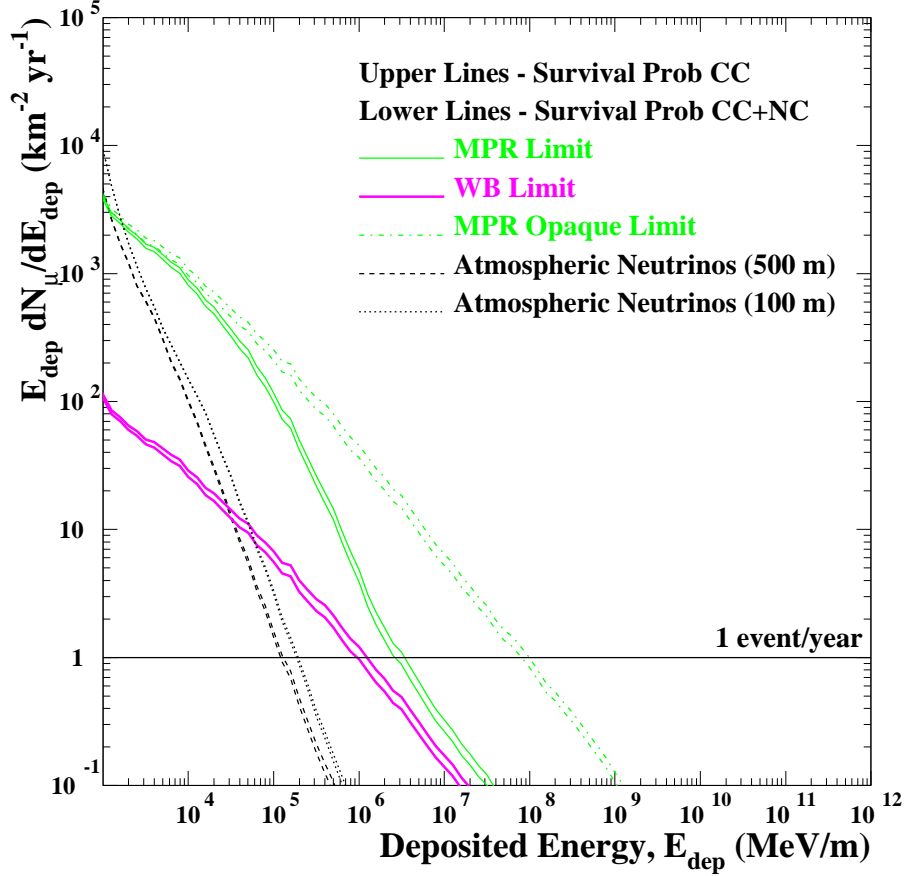


Fig. 14.— The spectral dependence on survival probability and path length. Neutral currents (NC) primarily affect the overall normalization of the hard spectra. The spectrum dependence on path-length is shown for the steep atmospheric background where the resolution tails become important. For 100 m paths there is a kink in the distribution. Without tails in the resolution, such a change in slope would signal the discovery of a new source of neutrinos. We use the 500 m resolution for our ideal detector and add the actual path length in Section 4 for real detectors.

a E^{-1} spectrum, cut-off by a gaussian shape with means varying from 3.0 to 11.5 $\log_{10}(\text{GeV})$, and widths of $\sigma = 0.3$. Their normalization varies between the MPR thin limit and WB limit. Figure 16 shows the muon fluxes for these sources as a function of deposited energy in the detector. From the numbers tabulated in Table 1 it is clear that the a km^2 detector will be sensitive to neutrino fluxes with incident energies between 10^5 and 10^7 GeV. Higher fluxes have been ruled out by the cosmic ray spectrum and lower fluxes are buried below the atmospheric background.

In the absence of signal events, flux limits can be set (D.E. Groom et al. 2000b; Feldman and Cousins 1998) based on the number of events observed, n_{obs} , by an experiment and knowledge of the mean background expected, b . The poisson probability that an observation is consistent with a mean signal, s is given by

$$P(n_{obs}|s) = (s + b)^{n_{obs}} \exp[-(s + b)] / n_{obs}! \quad (12)$$

Integrating this over all signals up to a confidence level, CL , gives the standard confidence belt, $s_{CL}(n_{obs}, b)$. Feldman and Cousins suggest that this belt be modified to avoid flip-flopping between one and two-sided intervals based on the experiment performed. Here we choose the simpler approach of always using a one-sided limit. The Feldman and Cousins approach leads to $\sim 10\%$ weaker limits for very low statistics experiments. The experimental flux limit is defined as

$$\Phi_{limit} = \phi_{s0} \times \frac{s_{CL}(n_{obs}, b)}{s}. \quad (13)$$

where ϕ_{s0} is the theoretical neutrino signal flux. Before the experiment is performed, there are no observed events. It is still interesting to determine the average $\langle s_{CL}(n_{obs}, b) \rangle$ of a collection of proposed experiments having only background events. (Hill et al. 2001)

$$\langle s_{CL}(n_{obs}, b) \rangle = \sum_{n_{obs}=0}^{\infty} s_{CL}(n_{obs}, b) P(n_{obs}|b) \quad (14)$$

We define the average limit that a detector can place on signal fluxes to be the sensitivity of the detector, $\Phi_{sensitivity}$.

$$\Phi_{sensitivity} = \phi_{s0} \times \frac{\langle s_{CL}(n_{obs}, b) \rangle}{s}. \quad (15)$$

The ratio ϕ_{s0}/s is the detection transfer function. The magnitude of the signal flux cancels in the ratio leaving only the sensitivity to the spectral shape.

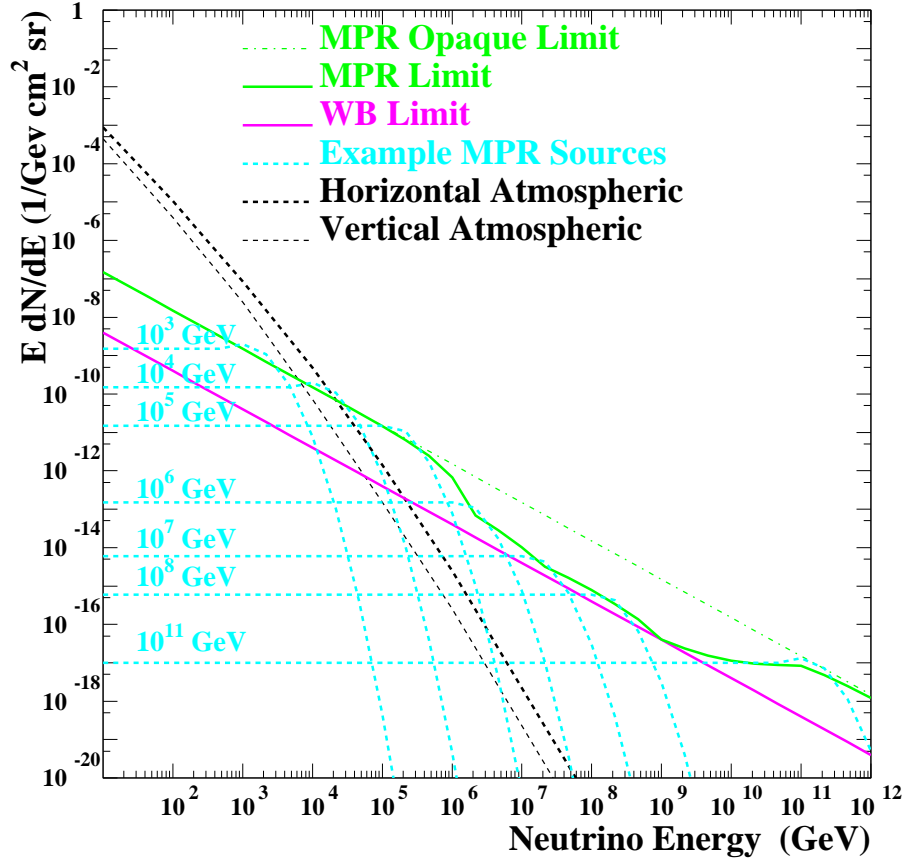


Fig. 15.— Possible sources making up the MPR flux. Sources are E^{-1} spectra cut-off by a gaussian of width 0.3. Amplitudes $\text{GeV}/(\text{cm}^2 \text{s sr})$ (cut-off energy(GeV)) 1.5×10^{-6} (10^3), 1.5×10^{-6} (10^4), 1.5×10^{-6} (10^5), 1.5×10^{-7} (10^6), 6.0×10^{-8} (10^7), 6.0×10^{-8} (10^8), and 1.0×10^{-6} (10^{11}).

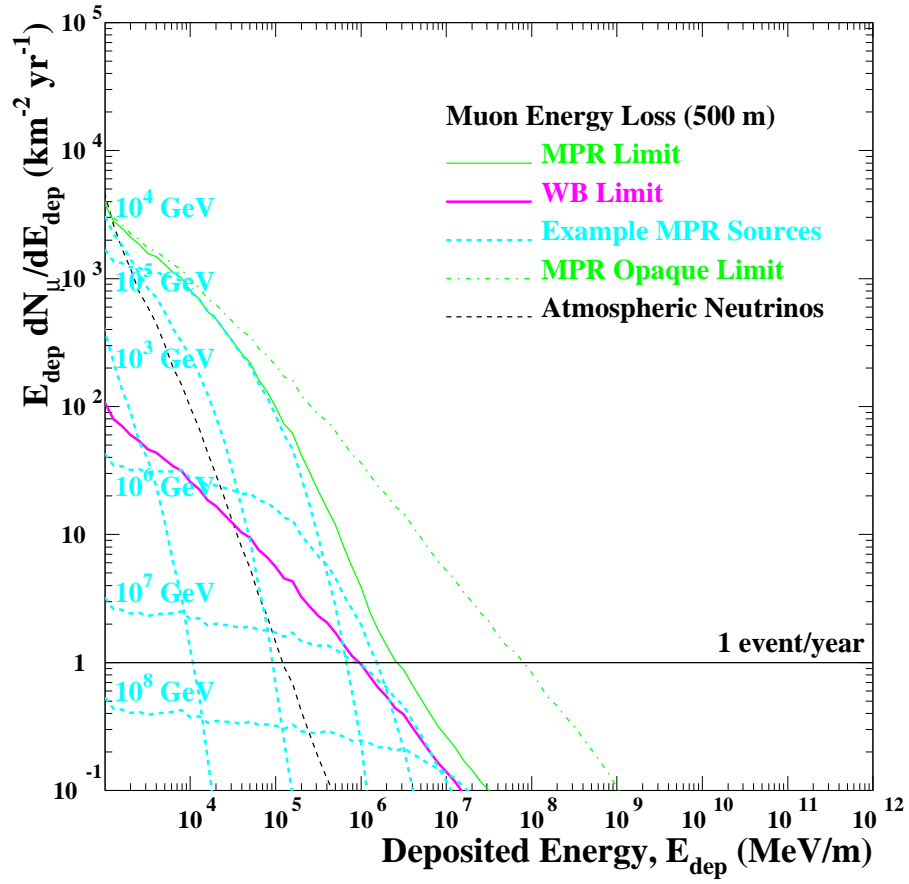


Fig. 16.— Muon flux as a function of energy deposited in the detector for a series of example sources that could make up the MPR flux.

3.4.1. Diffuse Limits

Table 2 shows the sensitivity (95% CL) of an ideal detector of km^2 incident area to neutrino fluxes and various spectral shapes as suggested in (Mannheim Protheroe and Rachen 2001). Included in these estimates are systematic uncertainties in the background normalization.

Systematic uncertainties affecting the background and signal bound our knowledge of the measurement. For example, an experiment that expects 1000 background events can easily discover a signal with 100 events, even with poisson sampling statistics. But this same experiment with a 10% uncertainty in the background is barely sensitive to a signal with 200 events. The limits quoted in Table 2 include Poisson statistics as described above, but limit the sensitive region to where the signal is larger than the 2σ uncertainty on the background.

We find that a detector with km^2 incident area will be sensitive to a spectral flux three times smaller than the WB limit. From the MPR sources, we can see that the limit is most sensitive to neutrinos of 1 PeV. Neutrinos between 10^5 and 10^7 contribute most to the signal rate.

3.4.2. Point Source Detection - GRB

One easy way to reduce the background in these experiments is to narrow the search bin from half the sky to the characteristic size of the detected angular resolution. The intrinsic resolution of a muon's direction with respect to the neutrino is about 1 square degree. In this way, we can divide half the sky into 20,628 one degree square patches of sky. There are two kinds of searches. The first involves looking for neutrinos from sources that are known to exist. The second involves looking for sources anywhere on the sky.

The GRB flux is a case where both the time and location of the burst is known *a priori*. In this case, we take all known bursts and search in one degree bins, coincident in time. The integrated GRB signal from Figure 13 is 15 events per year. The number of GRB detected in a year depends on the sensitivity of experiments like BATSE or MILAGRO. Based on expectations of these detectors, we estimate somewhere in the range of $10^2 - 10^3$ GRBs per year. Assuming that all 15 muons above were produced in some fraction of these GRBs, we find that the expected background in all GRB events is 0.015 muons. A 5σ discovery can be made even if the GRB flux is reduced by a factor of 5.

Somewhat surprising is the robustness of this result to variations in the number of detected GRBs and the time-scale of the event. Depending on the number of GRBs detected

by other experiments, the background can change by an order of magnitude. Similarly, if the neutrinos arrive over a 24 hour period instead of a 1 second pulse (used in the above calculation) then the background is 86,000 larger. In this case, the best limit comes from applying an energy cut at $10^{2.4}$ MeV/m which leaves only 0.012 background events and 13 GRB neutrino induced muons. If this energy cut is not possible, then the background is too large, and there is no way to find GRB muons that arrive on a long time scale.

3.4.3. Point Source Detection - AGN

The second point-source search involves looking for sources without prior knowledge of location or time. Here we reduce the up-going atmospheric neutrino background by 20,628 search bins on the sky. The signal is also divided among an unknown number of sources.

There is an art to choosing bins on the sky. If the bins are chosen before the experiment is performed, then sources will not fall in just one bin, and the search is not efficient. If sliding windows are used to find spots with the largest number of events, then the search is biased to the locations where the background has clustered. A poor-man's alternative is to consider a fixed array of search bins, but to perform 100 searches with each shifted by 1/10th of a degree in azimuth or zenith from the previous search. This is a close approximation to 100 independent searches of the sky. The signal will be 90% contained in at least one search, and can therefore be approximated by the true signal, ignoring the cases where the signal is partially contained in a different search. The effect is that instead of performing 20,628 experiments for each spot on the sky, we perform 2,062,800 experiments. To avoid mistaking a background fluctuation for signal, we calculate 6σ limits which will only be wrong one time out of 5 million.

If the diffuse flux is produced entirely from one point source, then an ideal km^2 detector will be sensitive to a flux $1.4 \times 10^{-9} \text{E}^{-2} \text{ GeV}/(\text{cm}^2 \text{ sr s})$ at 6σ . This is 28 times lower than the WB limit. Since the rate of neutrinos is expected to be about 5 times lower than the limit, we conclude that this rate is expected and easily detected. If, however, the flux is divided between 10 bright sources, then we will only be sensitive to a flux 2.8 times lower than WB, and a point source discovery would indicate new physics. This limit scales linearly with the number of sources that contribute to the flux; so, for example, 1042 sources are the maximum that may be detected by an ideal km^2 detector because more would violate the MPR Opaque Limit.

The diffuse limits have been treated as isotropic. From Figure 8, one can see that the diffuse flux ($10^5 - 10^7 \text{ GeV}$) is biased toward the horizon. Astronomy with neutrinos relies

on the flux being divided among a handful of bright point sources located within a few tens of degrees of the horizon.

4. Sensitivity of Proposed and Existing Detectors

The above calculations used an ideal geometry of a detector with km^2 incident area and 500 meters long for all zenith angles. We now include the geometry of proposed detectors to determine their acceptance. Combining the irreducible physics effects with the detector acceptance allows us to determine the best possible limit for such detectors.

Not included are the effects of specific detector designs which can only degrade the sensitivities. In real life detectors tend to be cylinders or spheres sunk into deep water, ice or caves. The interaction probability of the rock below or surrounding the detectors and the passive detecting medium of the instrument have to be considered. Particularly important effects which are not addressed in this paper are the number of sampling elements, the sensitivity of the detecting elements, the uniformity of the detecting medium, and the conversion of “deposited radiation” into a measurable light spectrum.

Figure 17 shows the geometrical profile of IceCube, AMANDA-II, ANTARES, NESTOR, and AMANDA-B10 as a function of zenith angle. Figure 18 shows the mean detector path length and efficiency assuming a reasonable minimum path length. IceCube is by far the largest, with essentially km^2 acceptance. AMANDA-II, ANTARES, and NESTOR are all of similar size and AMANDA-B10 is the smallest.

Table 3 lists the sensitivities of these detectors to an E^{-2} flux of high-energy neutrinos. These estimates include the effects of neutrino attenuation in the earth, muon transport, and fluctuations in energy deposition. For IceCube, a 300 m minimum track is required to reduce the systematic effects of the long tails in the resolution. For the others, a 100 m minimum track is required. For the smaller detectors, the irreducible systematic uncertainty is quite important. For IceCube, we use +24% for the atmospheric background systematic uncertainty, and for the others we use +50% (see section 3.4). Limits without systematics are 10% better for IceCube, and 30% better for the smaller detectors.

We state in section 2.4 that to ensure the discovery of neutrinos from astrophysical sources one needs a detector sensitive to about one fifth of the WB flux. We find that current and future detectors are at most sensitive to one third of the WB flux. IceCube will reach a sensitivity of one fifth the WB flux after 7-8 years of 100% efficient operation. To characterize the source luminosity or energetics we would need additional factors of 10-100 in rate. These detectors will be primarily useful as first-generation discovery instruments.

Muon Source Flux	Optimized Energy Cut (MeV/m)	Atmospheric Background, b (events)	Signal s (events)	Original Amplitude	Sensitivity km ² Amplitude (95% CL)
WB Opt Thin Limit	$10^{4.3}$	16.1	23.8	4.0×10^{-8}	1.3×10^{-8}
MPR Opt Thin Limit	$10^{4.3}$	16.1	487.	varies	$\times 0.016$
MPR Opaque Limit	$10^{4.3}$	16.1	893.	1.5×10^{-6}	1.3×10^{-8}
MPR Source (10^4 GeV)	$10^{4.3}$	16.1	36.4	1.5×10^{-6}	2.1×10^{-7}
MPR Source (10^5 GeV)	$10^{4.3}$	16.1	448.	1.5×10^{-6}	2.6×10^{-8}
MPR Source (10^6 GeV)	$10^{4.6}$	4.47	36.1	1.5×10^{-7}	2.2×10^{-8}
MPR Source (10^7 GeV)	$10^{5.0}$	0.83	4.31	6.0×10^{-8}	4.4×10^{-8}
MPR Source (10^8 GeV)	$10^{5.3}$	0.24	1.07	6.0×10^{-8}	1.4×10^{-7}

Table 2: Sensitivity of a km² detector to fluxes with a variety of spectral shapes.

Detector	Optimized Energy Cut (MeV/m)		Atmospheric Background, b (events)		WB Signal s (events)		Sensitivity (GeV/cm ² s sr)	
	90%	95%	90%	95%	90%	95%	90%	95%
IceCube	$10^{4.3}$	$10^{4.2}$	9.1	13.9	19.1	22.7	$1.1 \times 10^{-8} \text{E}^{-2}$	$1.4 \times 10^{-8} \text{E}^{-2}$
AMANDA-II	$10^{4.1}$	$10^{4.0}$	2.9	4.3	2.2	2.6	$6.5 \times 10^{-8} \text{E}^{-2}$	$8.0 \times 10^{-8} \text{E}^{-2}$
ANTARES	$10^{4.0}$	$10^{3.9}$	2.8	4.1	1.6	1.9	$8.7 \times 10^{-8} \text{E}^{-2}$	$1.1 \times 10^{-7} \text{E}^{-2}$
NESTOR	$10^{4.1}$	$10^{3.9}$	2.7	5.8	2.0	2.8	$7.0 \times 10^{-8} \text{E}^{-2}$	$8.2 \times 10^{-8} \text{E}^{-2}$
AMANDA-B10	$10^{3.9}$	$10^{3.7}$	2.8	5.4	1.2	1.7	$1.2 \times 10^{-7} \text{E}^{-2}$	$1.3 \times 10^{-7} \text{E}^{-2}$

Table 3: Sensitivity of existing and proposed detectors to fluxes with E^{-2} spectral shapes.

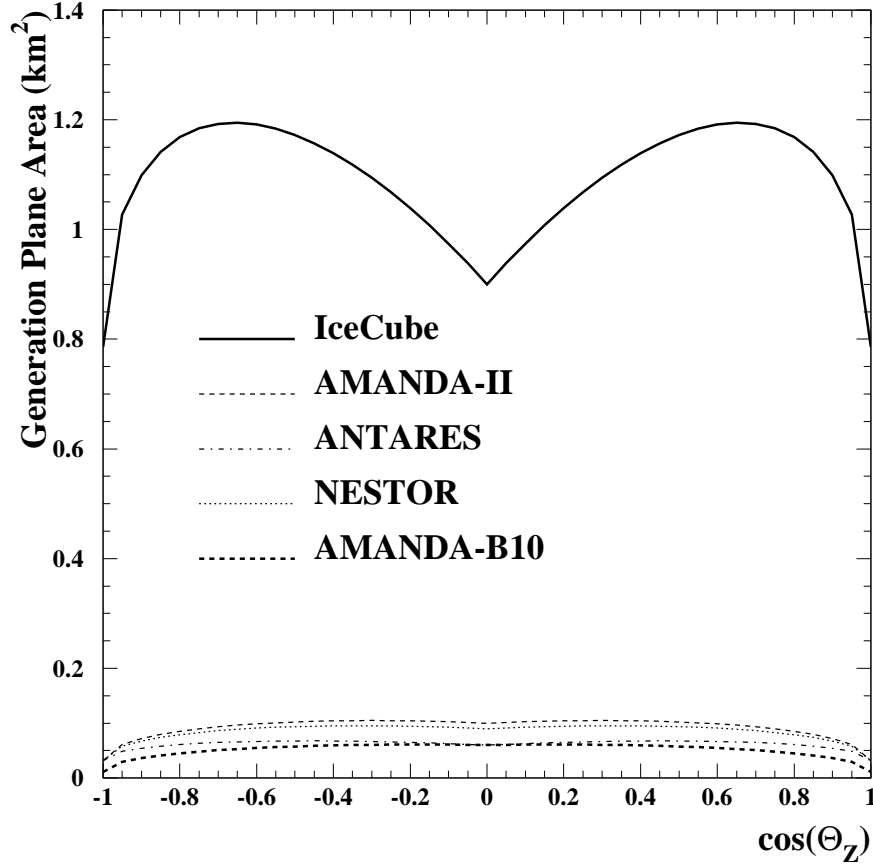


Fig. 17.— Geometrical dependence of the IceCube, ANTARES, NESTOR and AMANDA detectors as a function of zenith angle. Dimensions are for a cylinder of (depth, height, diameter) in meters: IceCube (1850, 900, 1000), AMANDA-II (1740, 500, 200), ANTARES (2250, 300, 200), NESTOR (3400, 450, 200), AMANDA-B10 (1740, 500, 120).

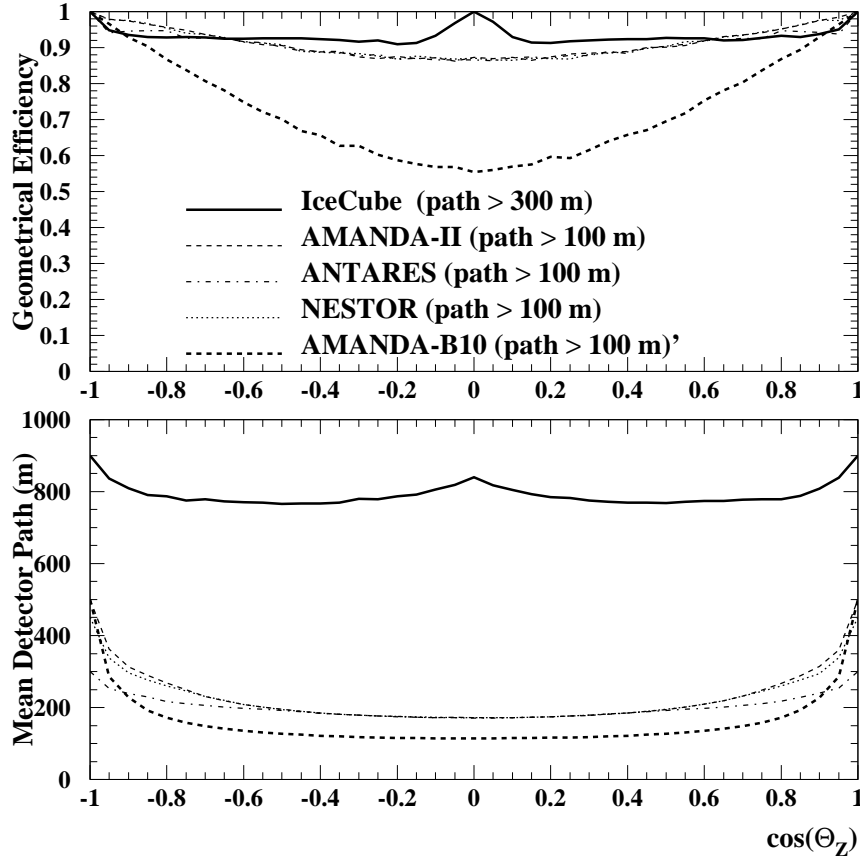


Fig. 18.— Geometrical efficiency for tracks longer than either 100 or 300 meters as a function of zenith angle.

5. Conclusions

We have summarized the muon neutrino plus muon anti-neutrino fluxes from astrophysical sources. We include fluxes predicted by models within the particle physics standard model and do not include the ones predicted by exotic models. In this way the muon neutrino flux is constrained by the Waxman and Bahcall limit (WB) (Waxman and Bahcall 1999) for energies above 10^6 GeV. The “thin source” (see 2.1.2) limit from Mannheim, Protheroe and Rachen (Mannheim Protheroe and Rachen 2001) can slightly loosen this limit for energies between 10^6 and 10^7 GeV and above 10^9 GeV. The “thick source” limit from these authors (Mannheim Protheroe and Rachen 2001) is shown to take into consideration sources that are unlikely to exist if they behave as expected by standard model physics. Any sources violating the thin limit must be modeled with physics beyond the standard model. These are in the exotic sources category and will be considered in a future analysis.

The neutrino signal is given by secondary muons produced in a charged current interaction of the neutrino with either the rock below the detector or the ice or water inside or surrounding the detector. We translate the muon neutrino event rate to a muon event rate and show our results in Figure 13.

From these rates we determine the sensitivity (see tables 2 and 3) for an ideal detector of Km^2 incident area as well as for current and proposed experiments (AMANDA-B10, AMANDA-II, NESTOR, ANTARES and IceCube).

Among the current experiments, AMANDA-B10 is the only one with a reported limit. At the 90% CL they find a limit of $0.9 \times 10^{-6} \text{E}^{-2} \text{ GeV}/(\text{cm}^2 \text{ sr s})$ (Hill et al. 2001). This limit is based on 137 days of live-time during 1997. For comparison, we find $2.7 \times 10^{-7} \text{E}^{-2} \text{ GeV}/(\text{cm}^2 \text{ sr s})$ at 90% CL for the same live-time statistics. This is consistent with their result if one considers that the instrument has additional resolution effects to be taken into consideration. The sensitivities listed in Table 3 are for 1 year of live-time and are more than 2 times lower.

The predicted sensitivity for Amanda-II is $7 \times 10^{-8} \text{E}^{-2} \text{ GeV}/(\text{cm}^2 \text{ sr s})$ for 2 years of operation (Barwick 2001). Assuming that two years would produce a better limit than one year, we conclude that the instrument has additional resolution issues. ANTARES predicts a sensitivity of $2 \times 10^{-7} \text{E}^{-2} \text{ GeV}/(\text{cm}^2 \text{ sr s})$ at 99.99% CL (5σ) (Montanet 1999). This is in agreement with our estimate which includes only irreducible physics and gross geometrical effects. The predicted sensitivity for IceCube at 90% CL is $9.5 \times 10^{-9} \text{E}^{-2} \text{ GeV}/(\text{cm}^2 \text{ sr s})$ (Leuthold and Wissing 2001) which agrees with our estimate if we calculate without systematic uncertainties. Since the Leuthold estimate includes a full detector simulation, we conclude that the detector comes close to the irreducible physical limit. It is important to

note that these predicted sensitivities are based on 100% duty cycles and do not include the dead time due to trigger, maintenance and other normal experimental procedures. We point out that our estimates are optimistic since we do not include additional degradation due to instrumental effects as described in the previous section.

The most promising flux to be measured is that from GRB neutrinos. The background in point-source searches is greatly reduced by spatial and temporal localization. Discovery of GRB neutrinos at the 5σ level is predicted to be possible in an ideal Km^2 detector according to current flux models. However, if there is no prior knowledge of location and time, detection of point sources relies on the flux being divided among a handful of bright sources located within a few tens of degrees of the horizon.

We state that a detector has to be designed to be sensitive to at least one fifth of the WB limit in order to ensure discovery of neutrinos from astrophysical sources. From all detectors analyzed, IceCube comes closest to this sensitivity, being able to measure a flux 3 times lower than the WB limit.

We thank Christopher Spitzer for his support in the numerical analysis, Dmitry Chirkin for his insight into muon radiation and Steve Barwick, Willi Chinowsky and Jozsef Ludvig for useful comments. We also thank NERSC for supporting the calculations in this paper with high-performance linux computing.

This work supported by NSF Grants KDI 9872979 and Physics/Polar Programs 0071886 and in part by the Director, Office of Energy Research, Office of High Energy and Nuclear Physics, Division of High Energy Physics of the U.S. Department of Energy under Contract No. DE-AC03-76SF00098 through the Lawrence Berkeley National Laboratory.

REFERENCES

- Albuquerque, I. F. M. and Smoot, G. F. 2001, *Phys. Rev. D*, 64, 053008
- Agrawal, V., Gaisser, T. K., Lipari, P. and Stanev, T. 1996, *Phys. Rev. D*, 53, 1314
- Bahcall, J. and Waxman, E. 1999, *astro-ph/9902383*
- Barwick, S. W. 2001, *Proceedings of the 27th International Cosmic Ray Conference*
- Bell, A. R. 1978, *MNRAS*, 182, 147
- Berezinsky, V. S. and Dokuchaev, V. I. 2001, *Astropart. Phys.* 15, 87

- Berezinsky, V. S., Gaisser, T. K., Halzen, F. and Stanev, T. 1993, *Astroparticle Phys.* 1, 281
- Blandford, R. D. and Ostriker, J. P. 1978, *ApJ*, 221, L29
- Chirkin, D. and Rhode, W. 2001, “Muon Monte Carlo: a New High-precision Tool for Muon Propagation Through Matter” ICRC 2001 proceedings.
- Dicus, D. A., Kretzer, S. Repko, W. W. and Schmidt, C. 2001, hep-ph/0103207
- Domokos, G. et al. 1993, *J. Phys. G: Nucl. Part. Phys.* 19, 899
- Dziewonski, A. 1989, *The Encyclopedia of Solid Earth Geophysics*, page 331, edited by James, D. E., Van Nostrand Reinhold, NewYork
- see references listed in <http://lhea-www.gsfc.nasa.gov/docs/gamcosray/EGRET/egret.html>
- Engel, R. and Stanev, T. 2001, astro-ph/0101216
- G. J. Feldman & R. D. Cousins 1998, *Phy. Rev. D.* 57, 7.
- T.Gaisser 1990, “Cosmic Rays and Particle Physics”, Cambridge University Press
- Gaisser, T. 2000, astro-ph/0011525, Proceedings of International Workshop on Observing Ultra-high energy Cosmic Rays from Space and Earth Puebla, Mexico
- Gaisser, T. K. and Stanev, T. 1985, *Phys. Rev. D*, 31, 2770
- Gandhi, R., Quigg, C., Reno, M. H. and Sarcevic, I. 1996, *Astropart. Phys.* 5, 81
- Gandhi, R., Quigg, C., Reno, M. H. and Sarcevic, I. 1998, *Phys. Rev. D*, 58, 093009
- Greisen, K. 1966 *Phys. Rev. Lett.*, 16, 748; Zatsepin, G. T. and Kuzmin, V. A. 1966 *JETP Lett.*, 4, 78
- Groom, D.E. et al. 2000, *The European Phys. Jour.* 15, section 23.6. pp 171-172.
- Groom, D.E. et al. 2000, *The European Phys. Jour.* 15, section 28. pp 195-201.
- Halzen, F. and Zas, E. 1997, *ApJ*, 488, 669
- Hettlage, C., Mannheim, K. and Learned, J. G. 2000, *Astropart.Phys.* 13, 45
- G.C. Hill et al. ”Search for a diffuse flux from sources of high energy neutrinos with AMANDA-B10” ICRC 2001 proceedings.
- Honda, M., Kajita, T., Kasahara, K. and Midorikawa, S. 1995, *Phys. Rev. D*, 52, 4985

The current status of the ICECUBE project is displayed at *pheno.physics.wisc.edu/icecube/*.

Inglemen, G. and Thunman, M. 1996, hep-ph/9604286

Kusenko, A. and Weiler, T. 2001, hep-ph/0106071

Learned, J. G. and Mannheim, K. 2000, Annual Rev. Nucl. Part. Science, 50, 679

Leuthold, M. and Wissing, H. “Performance Studies for the IceCube Detector” ICRC 2001 proceedings.

Lipari, P. and Stanev, T. 1991, Phys. Rev. D, 44, 3543

Macomb, D. J. et al. 1995, ApJ, 449, L99; 1996, ApJ459, L111

Mannheim, K. 1995, Astropart. Phys., 3, 295

Mannheim, K., Protheroe, R. J. and Rachen, J. P. 2001, Phys. Rev. D, 63, 023003

Montanet, F. et al. 1999, astro-ph/9907432

Piran, T. 1994, “Gamma-ray Bursts”, eds. Fishman, G. et al., AIP 307, NY

Protheroe, R. J. 1996, astro-ph/9607165

Rachen, J. P. and Meszaros, P. 1998, Phys. Rev. D58, 123005

Rhode, W. et al, 1996, Astroparticle Physics, 4 (1996) 217-225

Sikora, M., Begelman, M. C. and Rees, M. J., 1994, ApJ421, 153

Stecker, F, Done, C., Salamon, M. and Sommers, P. 1991, Phys. Rev. Lett., 66, 2697; 1992, Phys. Rev. Lett., 69, 2738(E)

Volkova, L. V. 1980, Yad. Fiz. 31, 1510. Also published at Sov. J. Nucl. Phys. 31, 784

Waxman, E. 1995, ApJ, 452, L1

Waxman, E. and Bahcall, J. 1997, Phys. Rev. Lett., 78, 2292

Waxman, E. and Bahcall, J. 1999, Phys. Rev. D, 59, 023002

Waxman, E. and Loeb, A. 2001, Phys. Rev. Lett., 87, 071101

Reference sheet for natbib usage

(Describing version 2.10 from 1997/11/24)

For a more detailed description of the `natbib` package, \LaTeX the source file `natbib.dtx`.

Overview

The `natbib` package is a reimplementation of the \LaTeX `\cite` command, to work with both author–year and numerical citations. It is compatible with the standard bibliographic style files, such as `plain.bst`, as well as with those for `harvard`, `apalike`, `chicago`, `astron`, `authordate`, and of course `natbib`.

Loading

Load with `\usepackage[options]{natbib}`. See list of *options* at the end.

Basic commands

The `natbib` package has two basic citation commands, `\citet` and `\citep` for *textual* and *parenthetical* citations, respectively. There also exist the starred versions `\citet*` and `\citep*` that print the full author list, and not just the abbreviated one. All of these may take one or two optional arguments to add some text before and after the citation.

<code>\citet{jon90}</code>	\Rightarrow	Jones et al. (1990)
<code>\citet[chap.~2]{jon90}</code>	\Rightarrow	Jones et al. (1990, chap. 2)
<code>\citep{jon90}</code>	\Rightarrow	(Jones et al., 1990)
<code>\citep[chap.~2]{jon90}</code>	\Rightarrow	(Jones et al., 1990, chap. 2)
<code>\citep[see][]{jon90}</code>	\Rightarrow	(see Jones et al., 1990)
<code>\citep[see][chap.~2]{jon90}</code>	\Rightarrow	(see Jones et al., 1990, chap. 2)
<code>\citet*{jon90}</code>	\Rightarrow	Jones, Baker, and Williams (1990)
<code>\citep*{jon90}</code>	\Rightarrow	(Jones, Baker, and Williams, 1990)

Multiple citations

Multiple citations may be made as usual, by including more than one citation key in the `\cite` command argument.

<code>\citet{jon90,jam91}</code>	\Rightarrow	Jones et al. (1990); James et al. (1991)
<code>\citep{jon90,jam91}</code>	\Rightarrow	(Jones et al., 1990; James et al. 1991)
<code>\citep{jon90,jon91}</code>	\Rightarrow	(Jones et al., 1990, 1991)
<code>\citep{jon90a,jon90b}</code>	\Rightarrow	(Jones et al., 1990a,b)

Numerical mode

These examples are for author–year citation mode. In numerical mode, the results are different.

<code>\citet{jon90}</code>	\Rightarrow	Jones et al. [21]
<code>\citet[chap.~2]{jon90}</code>	\Rightarrow	Jones et al. [21, chap. 2]
<code>\citep{jon90}</code>	\Rightarrow	[21]
<code>\citep[chap.~2]{jon90}</code>	\Rightarrow	[21, chap. 2]
<code>\citep[see][]{jon90}</code>	\Rightarrow	[see 21]
<code>\citep[see][chap.~2]{jon90}</code>	\Rightarrow	[see 21, chap. 2]
<code>\citep{jon90a,jon90b}</code>	\Rightarrow	[21, 32]

Suppressed parentheses

As an alternative form of citation, `\citealt` is the same as `\citet` but *without any parentheses*. Similarly, `\citealp` is `\citep` with the parentheses turned off. Multiple references, notes, and the starred variants also exist.

<code>\citealt{jon90}</code>	\Rightarrow	Jones et al. 1990
<code>\citealt*{jon90}</code>	\Rightarrow	Jones, Baker, and Williams 1990
<code>\citealp{jon90}</code>	\Rightarrow	Jones et al., 1990
<code>\citealp*{jon90}</code>	\Rightarrow	Jones, Baker, and Williams, 1990
<code>\citealp{jon90,jam91}</code>	\Rightarrow	Jones et al., 1990; James et al., 1991
<code>\citealp[pg.~32]{jon90}</code>	\Rightarrow	Jones et al., 1990, pg. 32
<code>\citetext{priv.\ comm.}</code>	\Rightarrow	(priv. comm.)

The `\citetext` command allows arbitrary text to be placed in the current citation parentheses. This may be used in combination with `\citealp`.

Partial citations

In author–year schemes, it is sometimes desirable to be able to refer to the authors without the year, or vice versa. This is provided with the extra commands

<code>\citeauthor{jon90}</code>	\Rightarrow	Jones et al.
<code>\citeauthor*{jon90}</code>	\Rightarrow	Jones, Baker, and Williams
<code>\citeyear{jon90}</code>	\Rightarrow	1990
<code>\citeyearpar{jon90}</code>	\Rightarrow	(1990)

Selecting citation style and punctuation

Use the command `\bibpunct` with one optional and 6 mandatory arguments:

1. the opening bracket symbol, default = (
2. the closing bracket symbol, default =)
3. the punctuation between multiple citations, default = ;
4. the letter ‘n’ for numerical style, or ‘s’ for numerical superscript style, any other letter for author–year, default = author–year;
5. the punctuation that comes between the author names and the year
6. the punctuation that comes between years or numbers when common author lists are suppressed (default = ,);

The optional argument is the character preceding a post-note, default is a comma.

Example 1, `\bibpunct{}{}{,}{a}{}{};` changes the output of

```
\citep{jon90,jon91,jam92}
```

into [Jones et al. 1990; 1991, James et al. 1992].

Example 2, `\bibpunct[;]{}{}{,}{a}{}{};` changes the output of

```
\citep[and references therein]{jon90}
```

into (Jones et al. 1990; and references therein).

Other formatting options

Redefine `\bibsection` to the desired sectioning command for introducing the list of references. This is normally `\section*` or `\chapter*`.

Redefine `\bibfont` to be a font declaration, e.g. `\small` to apply to the list of references.

The indentation after the first line of each reference is given by `\bibhang`; change this with the `\setlength` command.

The vertical spacing between references is set by `\bibsep`; change this with the `\setlength` command.

Automatic indexing of citations

If one wishes to have the citations entered in the `.idx` indexing file, it is only necessary to issue `\citeindextrue` at any point in the document. All following `\cite` commands, of all variations, then insert the corresponding entry to that file. With `\citeindexfalse`, these entries will no longer be made.

Sorting and compressing citations

Do not use the `cite` package with `natbib`; rather use one of the options `sort` or `sort&compress`.

These also work with author–year citations, making multiple citations appear in their order in the reference list.

Long author list on first citation

Use option `longnamesfirst` to have first citation automatically give the full list of authors.

Suppress this for certain citations with `\shortcites{key-list}`, given before the first citation.

Replacement bibliography styles

I provide three new `.bst` files to replace the standard L^AT_EX numerical ones:

```
plainnat.bst      abbrvnat.bst      unsrtnat.bst
```

Local configuration

Any local recoding or definitions can be put in `natbib.cfg` which is read in after the main package file.

Options that can be added to `\usepackage`

`round` (default) for round parentheses;

`square` for square brackets;

`curly` for curly braces;

`angle` for angle brackets;

`colon` (default) to separate multiple citations with colons;

`comma` to use commas as separators;

`authoryear` (default) for author–year citations;

`numbers` for numerical citations;

`super` for superscripted numerical citations, as in *Nature*;

`sort` orders multiple citations into the sequence in which they appear in the list of references;

`sort&compress` as `sort` but in addition multiple numerical citations are compressed if possible (as 3–6, 15);

`longnamesfirst` makes the first citation of any reference the equivalent of the starred variant (full author list) and subsequent citations normal (abbreviated list);

`sectionbib` redefines `\thebibliography` to issue `\section*` instead of `\chapter*`; valid only for classes with a `\chapter` command; to be used with the `chapterbib` package;

`nonamebreak` keeps all the authors' names in a citation on one line; causes overfull hboxes but helps with some `hyperref` problems.

Table 1: Additional AAST_EX symbols

\lesssim	<code>\lesssim, \la</code>	\gtrsim	<code>\gtrsim, \ga</code>
μm	<code>\micron</code>	---	<code>\sbond</code>
=	<code>\dbond</code>	=	<code>\tbond</code>
\odot	<code>\sun</code>	\oplus	<code>\earth</code>
\bigcirc	<code>\diameter</code>	\square	<code>\sq</code>
$^\circ$	<code>\arcdeg, \degr</code>	$''$	<code>\arcsec</code>
$'$	<code>\arcmin</code>	h	<code>\fh</code>
d	<code>\fd</code>	m	<code>\fm</code>
m	<code>\fm</code>	s	<code>\fs</code>
d	<code>\fdg</code>	f	<code>\farc</code>
m	<code>\farcs</code>	p	<code>\fp</code>
$\frac{1}{2}$	<code>\onehalf</code>	$UBVR$	<code>\ubvr</code>
$\frac{1}{3}$	<code>\onethird</code>	$U-B$	<code>\ub</code>
$\frac{2}{3}$	<code>\twothirds</code>	$B-V$	<code>\bv</code>
$\frac{1}{4}$	<code>\onequarter</code>	$V-R$	<code>\vr</code>
$\frac{3}{4}$	<code>\threequarters</code>	$U-R$	<code>\ur</code>

Table 2: Text-mode accents

\grave{o}	<code>\'{o}</code>	\bar{o}	<code>\={o}</code>	$\circ\circ$	<code>\t{oo}</code>
\acute{o}	<code>\' {o}</code>	\dot{o}	<code>\. {o}</code>	\textcircled{o}	<code>\c{o}</code>
\hat{o}	<code>\^{o}</code>	\ddot{o}	<code>\u{o}</code>	\textcircled{o}	<code>\d{o}</code>
\ddot{o}	<code>\" {o}</code>	\tilde{o}	<code>\v{o}</code>	\textcircled{o}	<code>\b{o}</code>
\tilde{o}	<code>\~{o}</code>	\textcircled{o}	<code>\H{o}</code>		

Table 3: National symbols

œ	<code>\oe</code>	å	<code>\aa</code>	ł	<code>\l</code>
Œ	<code>\OE</code>	Å	<code>\AA</code>	Ł	<code>\L</code>
æ	<code>\ae</code>	ø	<code>\o</code>	ß	<code>\ss</code>
Æ	<code>\AE</code>	Ø	<code>\O</code>		

Table 4: Math-mode accents

\hat{a}	<code>\hat{a}</code>	\dot{a}	<code>\dot{a}</code>
\check{a}	<code>\check{a}</code>	\ddot{a}	<code>\ddot{a}</code>
\tilde{a}	<code>\tilde{a}</code>	\breve{a}	<code>\breve{a}</code>
\acute{a}	<code>\acute{a}</code>	\bar{a}	<code>\bar{a}</code>
\grave{a}	<code>\grave{a}</code>	\vec{a}	<code>\vec{a}</code>

Table 5: Greek and Hebrew letters (math mode)

α	<code>\alpha</code>	ν	<code>\nu</code>
β	<code>\beta</code>	ξ	<code>\xi</code>
γ	<code>\gamma</code>	\omicron	<code>\o</code>
δ	<code>\delta</code>	π	<code>\pi</code>
ϵ	<code>\epsilon</code>	ρ	<code>\rho</code>
ζ	<code>\zeta</code>	σ	<code>\sigma</code>
η	<code>\eta</code>	τ	<code>\tau</code>
θ	<code>\theta</code>	υ	<code>\upsilon</code>
ι	<code>\iota</code>	ϕ	<code>\phi</code>
κ	<code>\kappa</code>	χ	<code>\chi</code>
λ	<code>\lambda</code>	ψ	<code>\psi</code>
μ	<code>\mu</code>	ω	<code>\omega</code>
\digamma	<code>\digamma</code>	\varkappa	<code>\varkappa</code>
ε	<code>\varepsilon</code>	ς	<code>\varsigma</code>
ϑ	<code>\vartheta</code>	φ	<code>\varphi</code>
ϱ	<code>\varrho</code>		
Γ	<code>\Gamma</code>	Σ	<code>\Sigma</code>
Δ	<code>\Delta</code>	Υ	<code>\Upsilon</code>
Θ	<code>\Theta</code>	Φ	<code>\Phi</code>
Λ	<code>\Lambda</code>	Ψ	<code>\Psi</code>
Ξ	<code>\Xi</code>	Ω	<code>\Omega</code>
Π	<code>\Pi</code>		
\aleph	<code>\aleph</code>	\beth	<code>\beth</code>
\gimel	<code>\gimel</code>	\daleth	<code>\daleth</code>

Table 6: Binary operators (math mode)

\pm	<code>\pm</code>	\cap	<code>\cap</code>
\mp	<code>\mp</code>	\cup	<code>\cup</code>
\setminus	<code>\setminus</code>	\uplus	<code>\uplus</code>
\cdot	<code>\cdot</code>	\sqcap	<code>\sqcap</code>
\times	<code>\times</code>	\sqcup	<code>\sqcup</code>
\ast	<code>\ast</code>	\triangleleft	<code>\triangleleft</code>
\star	<code>\star</code>	\triangleright	<code>\triangleright</code>
\diamond	<code>\diamond</code>	\wr	<code>\wr</code>
\circ	<code>\circ</code>	\bigcirc	<code>\bigcirc</code>
\bullet	<code>\bullet</code>	\bigtriangleup	<code>\bigtriangleup</code>
\div	<code>\div</code>	\bigtriangledown	<code>\bigtriangledown</code>
\triangleleft	<code>\triangleleft</code>	\triangleright	<code>\triangleright</code>
\vee	<code>\vee</code>	\odot	<code>\odot</code>
\wedge	<code>\wedge</code>	\dagger	<code>\dagger</code>
\oplus	<code>\oplus</code>	\ddagger	<code>\ddagger</code>
\ominus	<code>\ominus</code>	\amalg	<code>\amalg</code>
\otimes	<code>\otimes</code>	\unlhd	<code>\unlhd</code>
\oslash	<code>\oslash</code>	\unrhd	<code>\unrhd</code>

Table 7: AMS binary operators (math mode)

$\dot{+}$	<code>\dotplus</code>	\ltimes	<code>\ltimes</code>
\smallsetminus	<code>\smallsetminus</code>	\rtimes	<code>\rtimes</code>
\Cap	<code>\Cap, \doublecap</code>	\leftthreetimes	<code>\leftthreetimes</code>
\Cup	<code>\Cup, \doublecup</code>	\rightthreetimes	<code>\rightthreetimes</code>
$\bar{\wedge}$	<code>\barwedge</code>	\curlywedge	<code>\curlywedge</code>
\veebar	<code>\veebar</code>	\curlyvee	<code>\curlyvee</code>
\doublebarwedge	<code>\doublebarwedge</code>		
\boxminus	<code>\boxminus</code>	\circleddash	<code>\circleddash</code>
\boxtimes	<code>\boxtimes</code>	\circledast	<code>\circledast</code>
\boxdot	<code>\boxdot</code>	\circledcirc	<code>\circledcirc</code>
\boxplus	<code>\boxplus</code>	\centerdot	<code>\centerdot</code>
\divideontimes	<code>\divideontimes</code>	\intercal	<code>\intercal</code>

Table 8: Miscellaneous symbols

\dagger	<code>\dag</code>	\S	<code>\S</code>
\copyright	<code>\copyright</code>	\ddagger	<code>\ddag</code>
\P	<code>\P</code>	\pounds	<code>\pounds</code>
$\#$	<code>\#</code>	$\$$	<code>\\$</code>
$\%$	<code>\%</code>	$\&$	<code>\&</code>
$_$	<code>_</code>	$\{$	<code>\{</code>
$\}$	<code>\}</code>		

Table 9: Miscellaneous symbols (math mode)

\aleph	<code>\aleph</code>	\prime	<code>\prime</code>
\hbar	<code>\hbar</code>	\emptyset	<code>\emptyset</code>
\imath	<code>\imath</code>	∇	<code>\nabla</code>
\jmath	<code>\jmath</code>	\surd	<code>\surd</code>
ℓ	<code>\ell</code>	\top	<code>\top</code>
\wp	<code>\wp</code>	\bot	<code>\bot</code>
\Re	<code>\Re</code>	\parallel	<code>\parallel</code>
\Im	<code>\Im</code>	\angle	<code>\angle</code>
∂	<code>\partial</code>	\triangle	<code>\triangle</code>
∞	<code>\infty</code>	\backslash	<code>\backslash</code>
\Box	<code>\Box</code>	\diamond	<code>\Diamond</code>
\forall	<code>\forall</code>	\sharp	<code>\sharp</code>
\exists	<code>\exists</code>	\clubsuit	<code>\clubsuit</code>
\neg	<code>\neg</code>	\diamondsuit	<code>\diamondsuit</code>
\flat	<code>\flat</code>	\heartsuit	<code>\heartsuit</code>
\natural	<code>\natural</code>	\spadesuit	<code>\spadesuit</code>
\mho	<code>\mho</code>		

Table 10: AMS miscellaneous symbols (math mode)

\hbar	<code>\hbar</code>	\backprime	<code>\backprime</code>
\hslash	<code>\hslash</code>	\varnothing	<code>\varnothing</code>
\vartriangle	<code>\vartriangle</code>	\blacktriangle	<code>\blacktriangle</code>
\triangledown	<code>\triangledown</code>	\blacktriangledown	<code>\blacktriangledown</code>
\square	<code>\square</code>	\blacksquare	<code>\blacksquare</code>
\lozenge	<code>\lozenge</code>	\blacklozenge	<code>\blacklozenge</code>
\circledS	<code>\circledS</code>	\bigstar	<code>\bigstar</code>
\angle	<code>\angle</code>	\sphericalangle	<code>\sphericalangle</code>
\measuredangle	<code>\measuredangle</code>		
\nexists	<code>\nexists</code>	\complement	<code>\complement</code>
\mho	<code>\mho</code>	\eth	<code>\eth</code>
\Finv	<code>\Finv</code>	\diagup	<code>\diagup</code>
\Game	<code>\Game</code>	\diagdown	<code>\diagdown</code>
\Bbbk	<code>\Bbbk</code>	\restriction	<code>\restriction</code>

Table 11: Arrows (math mode)

\leftarrow	<code>\leftarrow</code>	\longleftarrow	<code>\longleftarrow</code>
\Lleftarrow	<code>\Lleftarrow</code>	\Longleftarrow	<code>\Longleftarrow</code>
\rightarrow	<code>\rightarrow</code>	\longrightarrow	<code>\longrightarrow</code>
\Rrightarrow	<code>\Rrightarrow</code>	\Longrightarrow	<code>\Longrightarrow</code>
\leftrightarrow	<code>\leftrightarrow</code>	\longleftrightarrow	<code>\longleftrightarrow</code>
\Leftrightarrow	<code>\Leftrightarrow</code>	\Longleftrightarrow	<code>\Longleftrightarrow</code>
\mapsto	<code>\mapsto</code>	\longmapsto	<code>\longmapsto</code>
\hookrightarrow	<code>\hookrightarrow</code>	\hookrightarrow	<code>\hookrightarrow</code>
\leftharpoonup	<code>\leftharpoonup</code>	\rightharpoonup	<code>\rightharpoonup</code>
\leftharpoondown	<code>\leftharpoondown</code>	\rightharpoondown	<code>\rightharpoondown</code>
\rightleftharpoons	<code>\rightleftharpoons</code>	\leadsto	<code>\leadsto</code>
\uparrow	<code>\uparrow</code>	\Updownarrow	<code>\Updownarrow</code>
\Uparrow	<code>\Uparrow</code>	\nearrow	<code>\nearrow</code>
\downarrow	<code>\downarrow</code>	\searrow	<code>\searrow</code>
\Downarrow	<code>\Downarrow</code>	\swarrow	<code>\swarrow</code>
\updownarrow	<code>\updownarrow</code>	\nwarrow	<code>\nwarrow</code>

Table 12: AMS arrows (math mode)

\dashleftarrow	<code>\dashleftarrow</code>	\dashrightarrow	<code>\dashrightarrow</code>
\leftrightsquigarrow	<code>\leftrightsquigarrow</code>	\rightleftarrows	<code>\rightleftarrows</code>
\leftrightsquigarrow	<code>\leftrightsquigarrow</code>	\rightleftarrows	<code>\rightleftarrows</code>
\Lleftarrow	<code>\Lleftarrow</code>	\Rrightarrow	<code>\Rrightarrow</code>
\twoheadleftarrow	<code>\twoheadleftarrow</code>	\twoheadrightarrow	<code>\twoheadrightarrow</code>
\leftarrowtail	<code>\leftarrowtail</code>	\rightarrowtail	<code>\rightarrowtail</code>
\looparrowleft	<code>\looparrowleft</code>	\looparrowright	<code>\looparrowright</code>
\leftrightharpoons	<code>\leftrightharpoons</code>	\rightleftharpoons	<code>\rightleftharpoons</code>
\curvearrowleft	<code>\curvearrowleft</code>	\curvearrowright	<code>\curvearrowright</code>
\circlearrowleft	<code>\circlearrowleft</code>	\circlearrowright	<code>\circlearrowright</code>
\Lsh	<code>\Lsh</code>	\Rsh	<code>\Rsh</code>
\upuparrows	<code>\upuparrows</code>	\downdownarrows	<code>\downdownarrows</code>
\upharpoonleft	<code>\upharpoonleft</code>	\upharpoonright	<code>\upharpoonright</code>
\downharpoonleft	<code>\downharpoonleft</code>	\downharpoonright	<code>\downharpoonright</code>
\multimap	<code>\multimap</code>	\rightsquigarrow	<code>\rightsquigarrow</code>
\leftrightsquigarrow	<code>\leftrightsquigarrow</code>		
\nleftarrow	<code>\nleftarrow</code>	\nrightarrow	<code>\nrightarrow</code>
\nLleftarrow	<code>\nLleftarrow</code>	\nRrightarrow	<code>\nRrightarrow</code>
\nleftarrow	<code>\nleftarrow</code>	\nLrightarrow	<code>\nLrightarrow</code>

Table 14: AMS binary relations (math mode)

\leq	<code>\leq</code>	\geq	<code>\geq</code>
\leqslant	<code>\leqslant</code>	\geqslant	<code>\geqslant</code>
\leqslantless	<code>\leqslantless</code>	\leqslantgtr	<code>\leqslantgtr</code>
\lesssim	<code>\lesssim</code>	\gtrsim	<code>\gtrsim</code>
\lessapprox	<code>\lessapprox</code>	\gtrapprox	<code>\gtrapprox</code>
\approx	<code>\approx</code>	\eqsim	<code>\eqsim</code>
\lessdot	<code>\lessdot</code>	\gtrdot	<code>\gtrdot</code>
\lll, \llless	<code>\lll, \llless</code>	\ggg, \gggtr	<code>\ggg, \gggtr</code>
\lessgtr	<code>\lessgtr</code>	\gtrless	<code>\gtrless</code>
\lesseqgtr	<code>\lesseqgtr</code>	\gtreqless	<code>\gtreqless</code>
\lesseqqgtr	<code>\lesseqqgtr</code>	\gtreqqless	<code>\gtreqqless</code>
\doteqdot, \Doteq	<code>\doteqdot, \Doteq</code>	\eqcirc	<code>\eqcirc</code>
\risingdotseq	<code>\risingdotseq</code>	\circeq	<code>\circeq</code>
\fallingdotseq	<code>\fallingdotseq</code>	\triangleq	<code>\triangleq</code>
\backsim	<code>\backsim</code>	\thicksim	<code>\thicksim</code>
\backsimeq	<code>\backsimeq</code>	\thickapprox	<code>\thickapprox</code>
\subseteq	<code>\subseteq</code>	\supseteq	<code>\supseteq</code>
\Subset	<code>\Subset</code>	\Supset	<code>\Supset</code>
\sqsubset	<code>\sqsubset</code>	\sqsupset	<code>\sqsupset</code>
\preccurlyeq	<code>\preccurlyeq</code>	\succcurlyeq	<code>\succcurlyeq</code>
\curlyeqprec	<code>\curlyeqprec</code>	\curlyeqsucc	<code>\curlyeqsucc</code>
\precsim	<code>\precsim</code>	\succsim	<code>\succsim</code>
\precapprox	<code>\precapprox</code>	\succapprox	<code>\succapprox</code>
\vartriangleleft	<code>\vartriangleleft</code>	\vartriangleright	<code>\vartriangleright</code>
\trianglelefteq	<code>\trianglelefteq</code>	\trianglerighteq	<code>\trianglerighteq</code>
\VDash	<code>\VDash</code>	\Vdash	<code>\Vdash</code>
\Vdash	<code>\Vdash</code>		
\smallsmile	<code>\smallsmile</code>	\shortmid	<code>\shortmid</code>
\smallfrown	<code>\smallfrown</code>	\shortparallel	<code>\shortparallel</code>
\bumpeq	<code>\bumpeq</code>	\between	<code>\between</code>
\Bumpeq	<code>\Bumpeq</code>	\pitchfork	<code>\pitchfork</code>
\varpropto	<code>\varpropto</code>	\backsim	<code>\backsim</code>
\blacktriangleleft	<code>\blacktriangleleft</code>	\blacktriangleright	<code>\blacktriangleright</code>
\therefore	<code>\therefore</code>	\because	<code>\because</code>

Table 13: Relations (math mode)

\leq	<code>\leq</code>	\geq	<code>\geq</code>
\prec	<code>\prec</code>	\succ	<code>\succ</code>
\preceq	<code>\preceq</code>	\succeq	<code>\succeq</code>
\ll	<code>\ll</code>	\gg	<code>\gg</code>
\subset	<code>\subset</code>	\supset	<code>\supset</code>
\subseteq	<code>\subseteq</code>	\supseteq	<code>\supseteq</code>
\sqsubset	<code>\sqsubset</code>	\sqsupset	<code>\sqsupset</code>
\sqsubseteq	<code>\sqsubseteq</code>	\sqsupseteq	<code>\sqsupseteq</code>
\in	<code>\in</code>	\ni	<code>\ni</code>
\vdash	<code>\vdash</code>	\dashv	<code>\dashv</code>
\smile	<code>\smile</code>	\mid	<code>\mid</code>
\frown	<code>\frown</code>	\parallel	<code>\parallel</code>
\neq	<code>\neq</code>	\perp	<code>\perp</code>
\equiv	<code>\equiv</code>	\cong	<code>\cong</code>
\sim	<code>\sim</code>	\bowtie	<code>\bowtie</code>
\simeq	<code>\simeq</code>	\propto	<code>\propto</code>
\asymp	<code>\asymp</code>	\models	<code>\models</code>
\approx	<code>\approx</code>	\doteq	<code>\doteq</code>
		\Join	<code>\Join</code>

Table 15: AMS negated relations (math mode)

\nless	\ngtr
\nleq	\ngeq
\nleqslant	\ngeqslant
\nleqq	\ngeqq
\lneq	\lneq
\lneqq	\lneqq
\lvertneqq	\lvertneqq
\lnsim	\lnsim
\lnapprox	\lnapprox
\nprec	\nsucc
\npreceq	\nsucceq
\precneqq	\succneqq
\precnsim	\succnsim
\precnapprox	\succnapprox
\nsim	\ncong
\nshortmid	\nshortparallel
\nmid	\nparallel
\nvdash	\nvDash
\nVDash	\nVDash
\ntriangleleft	\ntriangleright
\ntrianglelefteq	\ntrianglerighteq
\nsubseteq	\nsupseteq
\nsubseteqq	\nsupseteqq
\subsetneq	\supsetneq
\varsubsetneq	\varsupsetneq
\subsetneqq	\supsetneqq
\varsubsetneqq	\varsupsetneqq

Table 17: Delimiters (math mode)

$($	$($	$)$	$)$
$[$	$[$	$]$	$]$
$\{$	$\{$	$\}$	$\}$
\lfloor	\lfloor	\rfloor	\rfloor
\lceil	\lceil	\rceil	\rceil
\langle	\langle	\rangle	\rangle
$/$	$/$	\backslash	\backslash
$ $	$ $	$\ $	$\ $
\uparrow	\uparrow	\Uparrow	\Uparrow
\downarrow	\downarrow	\Downarrow	\Downarrow
\updownarrow	\updownarrow	\Updownarrow	\Updownarrow
\lrcorner	\lrcorner	\urcorner	\urcorner
\llcorner	\llcorner	\lrcorner	\lrcorner

Table 16: Variable-sized symbols (math mode)

\sum	\sum	\sum	\bigcap	\bigcap	\bigcap
\prod	\prod	\prod	\bigcup	\bigcup	\bigcup
\coprod	\coprod	\coprod	\bigsqcup	\bigsqcup	\bigsqcup
\int	\int	\int	\bigvee	\bigvee	\bigvee
\oint	\oint	\oint	\bigwedge	\bigwedge	\bigwedge
\odot	\odot	\odot	\bigotimes	\bigotimes	\bigotimes
\oplus	\oplus	\oplus	\biguplus	\biguplus	\biguplus

Table 18: Function names (math mode)

\arccos	\csc	\ker	\min
\arcsin	\deg	\lg	\Pr
\arctan	\det	\lim	\sec
\arg	\dim	\liminf	\sin
\cos	\exp	\limsup	\sinh
\cosh	\gcd	\ln	\sup
\cot	\hom	\log	\tan
\coth	\inf	\max	\tanh

Table 1. Percentage of Fake Stars Lost

Mag	Non-shell Stars			Shell Stars		
	F336W	F555W	F814W	F336W	F555W	F814W
20.25	2.2±7.4	0.9±6.8	...	0.0±44.7
20.75	2.4±7.8	...	2.8±7.4	1.7±6.6	...	1.4±6.7
21.25	0.1±7.7	...	1.7±7.6	2.6±6.5	...	0.9±6.6
21.75	2.4±4.5	2.2±7.4	0.1±7.6	7.1±4.5	0.9±6.8	3.3±6.5
22.25	3.4±3.1	1.8±7.7	2.9±4.4	11.8±3.6	0.4±6.6	5.7±4.4
22.75	4.5±2.9	1.8±7.7	4.7±3.1	26.2±3.6	3.4±6.5	10.9±3.6
23.25	7.0±2.4	3.4±4.5	3.7±2.9	44.2±3.3	10.7±4.5	20.6±3.5
More Data						
23.75	12.4±2.7	4.1±3.1	6.7±2.5	59.8±4.0	20.1±3.6	32.6±3.4
24.25	30.2±3.1	5.3±2.9	10.0±2.7	74.9±5.1	35.8±3.6	43.1±4.0
24.75	66.8±5.5	10.4±2.4	16.5±3.2	83.7±6.1	56.3±3.3	57.0±5.2
25.25	87.5±35.4	20.0±2.7	28.0±5.6	...	71.5±4.0	71.8±6.2
25.75	...	55.3±3.1	81.2±5.1	...
26.25	...	85.1±5.5	85.6±6.1	...
More Data						
27.75	12.4±2.7	4.1±3.1	6.7±2.5	59.8±4.0	20.1±3.6	32.6±3.4
28.25	30.2±3.1	5.3±2.9	10.0±2.7	74.9±5.1	35.8±3.6	43.1±4.0
29.75	66.8±5.5	10.4±2.4	16.5±3.2	83.7±6.1	56.3±3.3	57.0±5.2

Table 1—Continued

Mag	Non-shell Stars			Shell Stars		
	F336W	F555W	F814W	F336W	F555W	F814W
30.25	87.5±35.4	20.0±2.7	28.0±5.6	...	71.5±4.0	71.8±6.2
31.75	...	55.3±3.1	81.2±5.1	...
32.25	...	85.1±5.5	85.6±6.1	...
33.75	12.4±2.7	4.1±3.1	6.7±2.5	59.8±4.0	20.1±3.6	32.6±3.4
34.25	30.2±3.1	5.3±2.9	10.0±2.7	74.9±5.1	35.8±3.6	43.1±4.0
35.75	66.8±5.5	10.4±2.4	16.5±3.2	83.7±6.1	56.3±3.3	57.0±5.2
36.25	87.5±35.4	20.0±2.7	28.0±5.6	...	71.5±4.0	71.8±6.2
37.75	...	55.3±3.1	81.2±5.1	...
38.25	...	85.1±5.5	85.6±6.1	...